UNIVERSITY OF CALIFORNIA SAN DIEGO

A petrological and laser-ablation inductively coupled plasma mass spectrometry study of some volatile elements in unbrecciated eucrites

A thesis submitted in partial satisfaction of the
requirements for the degree Master of Science

in

Earth Sciences

by

Benjamin Kumler

Committee in charge:

Professor James M.D. Day, Chair
Professor Paterno Castillo
Professor Emily Chin

2020

The thesis of Benjamin Kumler is approved, and it is acceptable in quality and form for publication on microfilm and electronically:

_____

_____

_____

Chair

University of California San Diego

2020

TABLE OF CONTENTS

Signature Page iii

Table of Contents iv

List of Figures vi

List of Tables ix

Acknowledgements x

Abstract of the Thesis xi

1. Introduction 1

2. Methods 4

2.1. Sample Selection 4

2.2. Laser ablation inductively coupled plasma mass spectrometry 6

3. Results 10

3.1. Textural variations 10

3.2. Modal Percentages 20

3.3. Major Element Abundances 20

3.3.1 Pyroxene Grains 21

3.3.2 Plagioclase Grains 21

3.3.3 Fusion crust and ALHA 81001 22

3.4. Trace Element Abundances 22

3.4.1 Pyroxene Grains 23

3.4.2 Plagioclase Grains 33

3.4.3 Compositions of ALHA 81001 & Fusion Crust 44

3.4.4 Modal Reconstructions 47

4. Discussion 51

4.1. Assessment of primary crystallization products versus impact melts 51

4.2. Eucrite REE and incompatible trace element compositions for plagioclase and pyroxene 54

4.3. Analysis of modal reconstructions and comparison with bulk rock and fusion crust compositions 57

4.4. Abundances of the MVE (Cs, Zn, K, Rb, and Pb) in eucrites 59

5. Conclusions 67

6. Future Work 70

References 72

LIST OF FIGURES

Figure 1. Graphs of Stannern and Main Group trends, highlighting the samples studied 5

Figure 2. Parts per million values plotted as corrected by a single standard (NIST 610) versus data corrected using linear calibration of multiple standards 9

Figure 3. Plane polarized light image of ALHA 81001 10

Figure 4. Plane polarized light image of BTN 00300 11

Figure 5. Plane polarized light image of CMS 04049 12

Figure 6. Plane polarized light image of EET 90020 13

Figure 7. Plane polarized light image of GRA 98098 14

Figure 8. Plane polarized light image of LEW 85305 15

Figure 9. Plane polarized light image of NWA 1000. 16

Figure 10. Plane polarized light image of NWA 1923. 17

Figure 11. Plane polarized light image of PCA 91245. 18

Figure 12. Plane polarized light image of QUE 97053. 19

Figure 13. Incompatible trace element diagram for BTN 00300 pyroxene grains 23

Figure 14. Incompatible trace element diagram for CMS 04049 pyroxene grains 24

Figure 15. Incompatible trace element diagram for EET 90020 pyroxene grains 25

Figure 16. Incompatible trace element diagram for GRA 98098 pyroxene grains 26

Figure 17. Incompatible trace element diagram for LEW 85305 pyroxene grains 27

Figure 18. Incompatible trace element diagram for NWA 1000 pyroxene grains 28

Figure 19. Incompatible trace element diagram for NWA 1923 pyroxene grains 29

Figure 20. Incompatible trace element diagram for PCA 92145 pyroxene grains 30

Figure 21. Incompatible trace element diagram for QUE 97053 pyroxene grains 31

Figure 22. Incompatible trace element diagram of average pyroxene grain composition for each eucrite 32

Figure 23. Average pyroxene grain rare earth element diagram 33

Figure 24. Incompatible trace element diagram for BTN 00300 plagioclase grains 34

Figure 25. Incompatible trace element diagram for CMS 04049 plagioclase grains 35

Figure 26. Incompatible trace element diagram for EET 90020 plagioclase grains 36

Figure 27. Incompatible trace element diagram for GRA 98098 plagioclase grains 37

Figure 28. Incompatible trace element diagram for LEW 85305 plagioclase grains 38

Figure 29. Incompatible trace element diagram for NWA 1000 plagioclase grains 39

Figure 30. Incompatible trace element diagram for NWA 1923 plagioclase grains 40

Figure 31. Incompatible trace element diagram for PCA 92145 plagioclase grains 41

Figure 32. Incompatible trace element diagram for QUE 97053 plagioclase grains 42

Figure 33. Incompatible trace element diagram of average plagioclase grain composition for each eucrite 43

Figure 34. Rare earth element diagram for average plagioclase grain compositions in eucrites 44

Figure 35. Incompatible trace element diagram for spots measured in the eucrite ALHA 81001 45

Figure 36. Rare earth element diagram for spots measured in the eucrite ALHA 81001 45

Figure 37. Incompatible trace element diagram for average ALHA 81001 versus average fusion crust compositions measured for BTN 00300, EET 90020, and LEW 85305 46

Figure 38. Modal reconstruction of BTN 00300 48

Figure 39. Modal reconstruction of EET 90020 49

Figure 40. Modal reconstructions for LEW 85305 50

Figure 41. Modal Reconstruction of QUE 97053 50

Figure 42. Modal reconstructions for NWA 1923 51

Figure 43. Incompatible trace element diagram for plagioclase grains in average granular eucrites, average subophitic eucrites, and NWA 1000 53

Figure 44. Incompatible trace element diagram for pyroxene grains in average granular eucrites, average subophitic eucrites, and NWA 1000 54

Figure 45. Incompatible trace element diagram showing average plagioclase and pyroxene grain compositions for each eucrite 55

Figure 46. Left: Rb/Ba diagram of lunar volcanic glass. Right: Rb/Ba diagram of plagioclase grains measured in this study 60

Figure 47. Rubidium/Sr diagram of plagioclase and pyroxene measured in this study 61

Figure 48. Left: Zinc/Fe diagram of pyroxenes from eucrite samples in this study. Right: Zn/Fe diagram showing MORB & OIB data, lunar volcanic glass, plagioclase and pyroxene samples in this study, and bulk eucrite data 63

Figure 49. Volatility trend graph of 50% condensation temperature versus elemental abundance normalized to CI chondrite and Si 64

Figure 50. Volatility trend graph of bond energy versus elemental abundance normalized to CI chondrite and Si 65

LIST OF TABLES

Table 1. 50% condensation temperatures and bond energies of a selection of elements 2

Table 2. Chart of measured modal abundances from this study 20

Table 3. Major Element Abundances – wt. % oxide 21

Table 4. Major Element Abundances for fusion crust and ALHA 81001 – wt. % oxide 22

Table 5. Plagioclase and pyroxene model percentages 47

ACKNOWLEDGEMENTS

This project would not have happened without help from so many people. Thank you primarily to my advisor, James Day, for his patience, knowledge, and guidance throughout this project. Thank you to Ruan Hattingh, for his help with the LA-ICP-MS machine. Thank you to Jasmeet Dhaliwal for all of the bulk data in this study, and the previous research into understanding these samples better, which I benefited from greatly. Thank you to Kim Tait for analyzing some extra samples to make my corrections better. Thank you to Jacques Lyakov for the program to process the data coming off the LA-ICP-MS machine, which saved many hours of work. Thank you to the rest of the Scripps Isotope Geochemistry Lab for their friendship, good conversation, support and motivation: Eric, Nicole, Jen, Carrie, Brian, Emily, Marine, and Brendon. And thank you to professors Pat Castillo and Emily Chin for their patience and agreeing to be on my committee.

Thank you to my parents, Mark and Brigid, for their endless support, harassment (motivation), encouragement, questions, love, and patience. Thank you to my Grandma Rosemary, for her support and prayers. Thank you to my Grandma Judy, for her words of encouragement. Thank you to my wonderful girlfriend, Jenna, for her support and motivation. And thank you to my siblings, all of my other friends, and teammates for the support, encouragement, competition, and keeping me sane over the years.

The process of this project coincided with events that have highlighted the inequity and injustice still prevalent in this country and the world. I would like to acknowledge my inherent privilege and voice support for all those still fighting for the same rights that I enjoy.

ABSTRACT OF THE THESIS

A petrological and laser-ablation inductively coupled plasma mass spectrometry study of some volatile elements in unbrecciated eucrites

by

Benjamin Kumler

Master of Science in Earth Sciences

University of California San Diego, 2020

Professor James M.D. Day, Chair

Polished thin sections of ten eucrites, meteorites originating from the asteroid Vesta, were examined using polarized light microscopy, photomicrograph mapping, and Laser Ablation Inductively Coupled Plasma Mass Spectrometry (LA-ICP-MS) to investigate their compositions, with particular emphasis on elements known to be volatile at planetary formation conditions. The samples were assessed for pristinity and grouped into impact melts, granular, and subophitic textures. LA-ICP-MS analysis was performed on selected samples for individual pyroxene and plagioclase grains – the main silicate phases - as well as fusion crust, to measure major and trace element abundances, with an emphasis on moderately volatile elements

(MVE's) such as Cs, Zn, K, Rb, and Pb. Incompatible trace element abundances are in generally good agreement between samples, and both plagioclase and pyroxene grains show depletions in the MVE's. Modal reconstructions were done using plagioclase and pyroxene and compared to bulk rock data. They fairly accurately recreate the bulk rock, besides the most incompatible elements, which must exist in minor accessory minerals known to occur in eucrites (e.g., apatite, zircon, baddeleyite). Fusion crust measurements, along with ALHA 81001 (a fine-grained impact melt,) are almost identical to the bulk rock data, confirming their usefulness as a proxy for bulk rock composition. Volatile abundances were assessed using Rb/Ba, Rb/Sr, and Zn/Fe ratios, which compare an MVE to a refractory element. These show eucrites having similar levels of volatile depletion to the Moon. Finally, normalized elemental abundances were plotted versus the element's volatility, in which volatile elements fall along a downward trend, with the slope indicating the level of volatiles present. From this perspective, eucrite volatile abundances fall in between those of the Earth and the Moon.

1. Introduction

Eucrites are part of the HED (Howardite, Eucrite, Diogenite) suite of meteorites. These stony achondrites are thought to originate from the crust of the asteroid 4-Vesta (Binzel and Xu, 1993; McSween et al., 2013; McSween et al., 2010; Mittlefehldt, 2015; McCord et al., 1970), and have some of the earliest crystallization ages in the Solar System at about 4.56 Ga (Lugmair and Shukolyukov, 1998; Trinquier et al., 2008, Bogard and Garrison, 2003). With an average diameter of 525 km, and mass of 2.59×10^{20} kg, Vesta is one of two large asteroids (the other being Ceres) in the asteroid belt, and is particularly useful for study because it appears to be differentiated (Barrat et al., 2000; Hublet et al., 2017; Mayne et al., 2009), and so would be one of few protoplanets that has survived from the early Solar System. Multiple hypotheses exist to explain the formation and differentiation of Vesta, and which aspects of its structure are represented by the different members of the HED suite. One common hypothesis is that the formation and differentiation of Vesta involved crystallization from a magma ocean (Barrat et al., 2000; Righter and Drake, 1997; Mandler and Elkins-Tanton, 2013; Elkins-Tanton, 2012.) However, geochemical and geophysical arguments also support partial melting from a mostly solid mantle, without the requirement of a magma ocean (Dhaliwal et al., in review; Stolper, 1977; Neumann et al., 2014). In all hypotheses, eucrites are considered to represent a volcanic component of the Vestan crust. The composition of eucrites is basaltic, composed primarily of plagioclase and pyroxene, with minor accessory minerals (Mayne et al., 2009; De Sanctis et al., 2012) such as spinel, ilmenite, silica, metal, sulfide, apatite, zircon and baddeleyite (Dhaliwal et al., in review; Mayne et al., 2009). This study measures major and trace element data from individual plagioclase and pyroxene grains to examine the abundance and distribution of

moderately volatile elements (see Table 1: elements with 50% condensation temperatures below 1150K, or below that of Lithium; Lodders, 2003). In addition to minimizing risk of measuring contaminated material, which can exist in cracks, veins, and on the edges of or in between minerals, especially in meteorites, measuring individual phases has the potential to reveal the distribution of elements in eucrites. Since eucrites are dominantly composed of plagioclase and pyroxene, they also enable assessment of reconstruction of the bulk rock based on these measurements, and where missing components might be in trace phases.

Table 1. 50% condensation temperatures (Lodders, 2003) and bond energies (Albarède et al., 2014) of a selection of elements.

		50% T_C (K)	Bond Energy (kJ/mol)
Refractory	Zr	1741	579
	Th	1659	526
	Al	1653	501.9
	U	1610	472
	La	1578	415
	Ca	1517	402.1
	Ce	1478	473
	Sr	1464	426.3
	Ba	1455	
Transitional	Mg	1336	358.2
	Si	1310	454
	Li	1142	340.5
Moderately Volatile	K	1006	271.5
	Na	958	270
	Rb	800	276
	Cs	799	293
	Pb	727	181
	Zn	726	224.8
Highly Volatile	Br	546	194
	I	535	152
	O	180	50
	N	123	30
	Xe	68	6
	C	40	9.1

Contamination is always a concern when studying meteorites, since they are inevitably spalled to Earth as the result of an impact, which may introduce pieces of the impactor or regolith from other locations on the parent body. Additionally, most meteorites found on Earth are exposed to the elements, especially in hot desert finds, or other places for long periods of time before being found, introducing abundant potential for terrestrial alteration (Crozaz & Wadhwa, 2001; Crozaz et al., 2003; Mittlefehldt and Lindstrom, 1991; Hyde et al., 2014). An important part of this study, therefore, involves determining which samples may have undergone some alteration, and which are the most pristine. Brecciated samples were precluded from study, as were unbrecciated meteorites that showed signs of brecciation or alteration. Additionally, bulk rock HSE abundances were analyzed as another sign of potential contamination (Day et al., 2016).

During the formation and condensation of the Solar System, elements behave differently according to fundamental characteristics, such as how volatile or refractory they are (see Table 1). Volatile elements and compounds such as Cl, Br, I, Zn, H_2O, CH_4, and NH_3, are important to the differentiation and evolution of planets, as well as to life on Earth. Their location within the Solar System during planetary accretion likely controlled baseline volatile abundances for planetary bodies (Day, 2015) but many mechanisms of volatile loss also play a role in their current volatile element abundances (Dhaliwal et al., 2018). When volatile abundances are low and hard to measure, moderately volatile elements (MVE's) are more abundant, and can be used as tracers to assess volatile abundances. Using ratios between volatile and refractory elements, as well as the volatility trend visible when plotting normalized elemental abundances versus a measure of the element's volatility (Albarède et al., 2014), this study will constrain the volatile abundances of eucrites, and compare them to Earth and the Moon.

2. Methods

In this study polished thin sections were examined using polarized light microscopy and measured for major- and trace-element abundances using Laser Ablation Inductively Coupled Plasma Mass Spectrometry (LA-ICP-MS).

2.1. Sample Selection

Twenty-one eucrite polished sections were examined using polarized light microscopy and photomicrograph mapping. After petrographic description of samples, and a cross-check with the Meteoritical Bulletin Database, brecciated and polymict samples were precluded from further study, and only 'unbrecciated' samples were studied for their MVE contents. Samples were further high-graded by limitations of the LA-ICP-MS analysis to be done; fine-grained samples with the not enough mineral phases larger than ~100 um in size were avoided, to ensure that the laser would only measure a single phase at the scale of laser spot diameter (100 μm).

Bulk rock major- and trace-element data for all samples are from Dhaliwal et al. (in review). Highly siderophile element (HSE) abundances were plotted for each sample, and samples with extremely high abundances of these elements, or other evidence for contamination, were precluded from further study. Many of these were samples previously precluded for being brecciated or polymict eucrites, supporting the concept that these samples have experienced meteoritic contamination.

Bulk rock data was used to produce La versus FeO(t)/MgO and La versus Sc graphs, such as Figure 1, which illustrates the differences between the Stannern and Main (Nuevo Laredo) trends, as most recently defined by Barrat et al. (2007). The final samples selected for

study span the major trends enabling assessment of similarities or differences in MVE abundances. This ultimately led to one deviation from our filtration routine, which was the inclusion of eucrite ALHA 81001, even though it was fine-grained, and this will be discussed later.

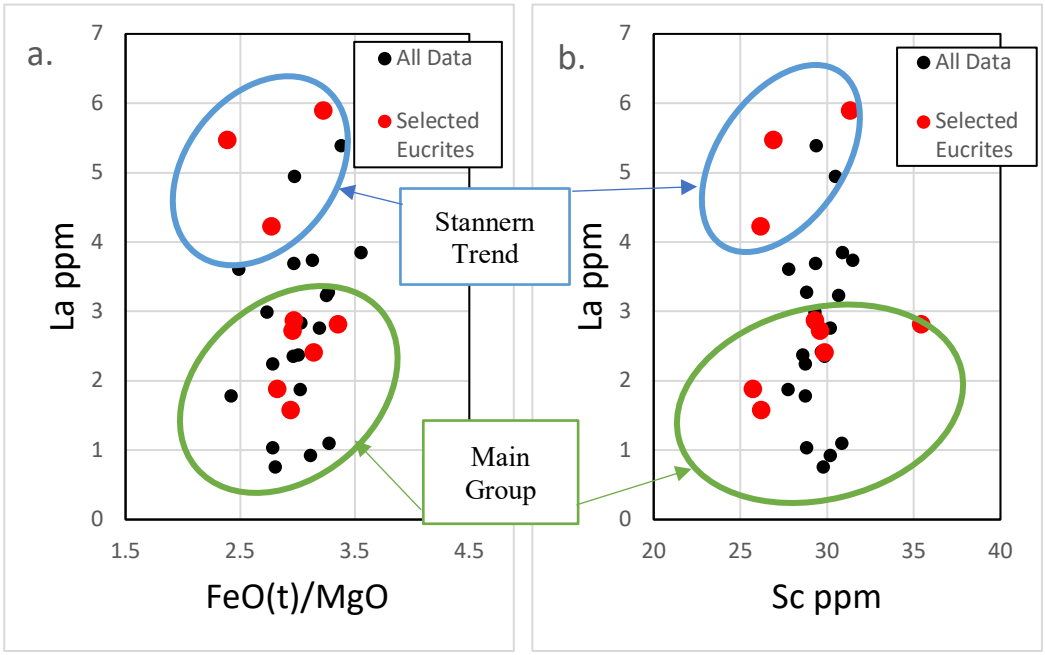

Figure 1. Graphs of Stannern and Main Group trends, highlighting the samples studied. Data from Dhaliwal (in review) and Stannern and Main group trends are taken from Barrat et al. (2007).

The final list of ten samples selected for further study in this project is as follows: Allan Hills (ALHA) 81001, Bates Nunataks (BTN) 00300, Cumulus Hills (CMS) 04049, Graves Nunatak (GRA) 98098, Lewis Cliff (LEW) 85305, Northwest Africa (NWA) 1000, NWA 1923, Pecora Escarpment (PCA) 91245, and Queen Alexandra Range (QUE) 97053. Modal percentages were calculated using photomicrograph maps constructed by multiple imaging of the sections, and cropped to isolate the main portion of the sample. Using photo editing software, the images were converted to grayscale, and thresholding was used to isolate each mineral phase based on how light or dark it appears. Modal percentages were calculated by

dividing this area by the total area of the sample and were performed independently by the author (BK) as well as James Day, to confirm quality assurance.

2.2. Laser ablation inductively coupled plasma mass spectrometry

The main approach in this study was to analyze polished thin sections of unbrecciated eucrites using Laser Ablation Inductively Coupled Plasma Mass Spectrometry (LA-ICP-MS). Grains of plagioclase and pyroxene were measured, along with fusion crust, where present and of sufficient surface area to measure. The main phases found in eucrites were analyzed, rather than oxides, metals, phosphates or sulfides. This was done for two reasons: first, analyses of plagioclase and pyroxene allow for direct comparison between samples, and second, not all minor phases are present, or of sufficient size, in eucrite meteorites, for similar direct comparison. The photomicrograph sample maps were examined and, prior to LA-ICP-MS, locations were selected, with roughly 10 spots each of pyroxene and plagioclase to measure. The spots were selected based on the mineral being large enough to be measured with a 100 um laser spot, to examine a variety of locations around the sample, and to include any visual variation in the phases, e.g., both light and dark pyroxenes in samples that had these discolored phases. If fusion crust was present in the sample, about five spots on the fusion crust were also measured.

The selected spot locations were then measured with a New Wave Research (NWR) UP213 Laser Ablation System coupled to a Thermo Fisher Scientific™ iCAP™ Qc ICP-MS instrument. A standard laser spot size of 100 μm, with a 5 Hz repetition rate was used, and the laser energy output percentage, typically around 44%, was modified slightly to obtain a target fluence of between 3 and 3.5 J/cm^2. Reference standards, including artificially created glasses,

were measured in the same run, with each standard measured at least twice each before and twice after the sample was measured, to enable accurate and precise correction of the data. The standards chosen were NIST612, NIST610, BHVO-2g, BCR-2g, and BIR-1g, all commonly used when analyzing silicate minerals because they span a range of trace-element compositions. Additionally, NIST 610 was measured once or twice roughly halfway through the sample measurements, to confirm no major sensitivity drift during analyses. The isotopes measured for all samples were ^{7}Li, ^{29}Si, ^{39}K, ^{44}Ca, ^{45}Sc, ^{57}Fe, ^{66}Zn, ^{85}Rb, ^{88}Sr, ^{89}Y, ^{90}Zr, ^{93}Nb, ^{133}Cs, ^{137}Ba, ^{139}La, ^{140}Ce, ^{141}Pr, ^{146}Nd, ^{147}Sm, ^{153}Eu, ^{157}Gd, ^{159}Tb, ^{163}Dy, ^{165}Ho, ^{166}Er, ^{169}Tm, ^{172}Yb, ^{175}Lu, ^{178}Hf, ^{208}Pb, ^{232}Th, and ^{238}U, and these data were then corrected to total elemental abundances.

For each spot, measurements were taken for a total of 60 seconds. Background measurements were taken for the first 20 seconds, while the laser was firing, but not ablating the sample. At 20 seconds, the laser shutter was opened, enabling ablation of the sample. This resulted in the intensity in counts per second (cps) for the selected elements to rapidly rise to a steady value, where it stayed for the remaining 35-40 seconds. Laser ablation and background characteristics were manually checked for each spot, typically with 0-15 seconds being used as the background, and 30-60 seconds being used as the sample measurement. All of the data from each of these intervals was averaged after aberration correction (see below), and then the background value was subtracted from the sample value to give the actual intensity from the sample.

Several spot analyses exhibited unusual intensity patterns that would change midway through analyses, would slowly ramp up over the run, or would show spikes in certain elements up to several orders of magnitude above the median measurement value. Patterns showing a few spikes in an otherwise level and stable elemental pattern were the most common of these

unusual patterns. These can be interpreted as the laser penetrating and measuring tiny inclusions of other minerals or metals within the main mineral grain of interest, which had concentrations of particular elements (e.g., Fe) orders of magnitude higher than the intended mineral. Since these outlier data points would throw off the averages, and do not represent the chemistry of the intended mineral, these points were removed from the dataset and are referred to here as the aberration correction.

Patterns that changed midway through, with some elements decreasing while others increased, reflect laser penetration through the intended mineral into a different mineral underneath. In this instance, when there was enough data (>15 seconds) for each mineral, the measurement for each mineral was recorded and analyzed separately. For patterns that slowly ramped up in intensity, indicating an issue with gas flow in the ablation cell, a second spot was attempted on the mineral. If this spot exhibited the same behavior, both spots were rejected.

Intensity data was corrected to silicon because it is the most abundant measurable element in both plagioclase and pyroxene and had a constant value in all grains of each mineral. Calcium and iron, the other common elemental correction options, can vary by up to 15 weight percent between high-Ca and low-Ca pyroxenes (Mayne et al., 2009). Silicon concentrations were taken from Mayne et al. (2009) and Dhaliwal et al. (in review). For NWA 1000 and NWA 1923, silicon concentrations were taken from new and unpublished electron microprobe data collected by Kim Tait. Two measurements were taken adjacent to each laser ablation pit from this study's laser ablation work, and the average of those electron microprobe silicon measurements was used to correct each spot individually. Concentrations of the reference standards were taken from the preferred values on GeoReM: A New Geochemical Database for Reference Materials and Isotopic Standards. The data was initially corrected both using just

NIST 610, since it was measured an additional one or two times midway through running the sample. The data were also corrected linearly using the calibration curves constructed from NIST 612, NIST 610, and BHVO-2g. These three standards bracketed the data and created a strong linear correlation (average r-squared value of 0.996 ± 0.005) for all elements, except calcium. This is because Ca only varies from 7.06 to 13.3 weight percent between the three standards, while Sr, for example, varies from 39 to 460 ppm. To compare these two techniques, these values were plotted against each other in Figure 2 shown below. As seen in this figure, the values agree closely, with a slight offset towards the linear axis, showing slightly lower values with the linear correction. Additionally, values corrected to only one standard were divided by the linearly corrected values, giving an average of 0.984 ± 0.059. The linearly corrected values are used for all data in this study because they are tied to more reference standards and so are deemed as more accurate.

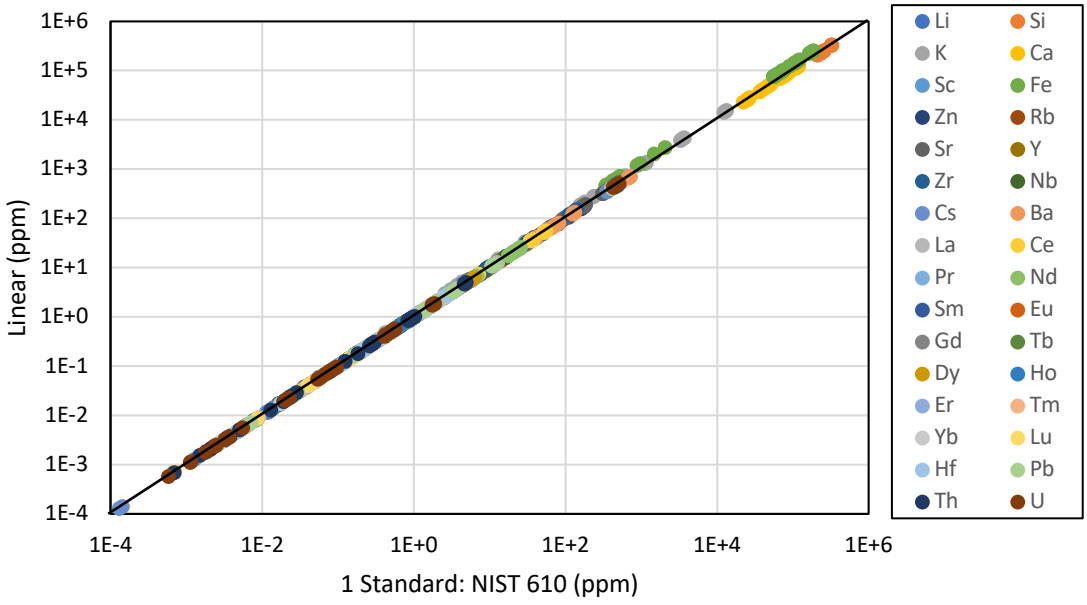

Figure 2. Parts per million values plotted as corrected by a single standard (NIST 610) versus data corrected using linear calibration of multiple standards.

3. Results

3.1. Textural variations

Allan Hills 81001 has a fine-grained matrix, with acicular crystals of pyroxene and a variolitic texture (Figure 3). It has elongated, feathery pyroxenes up to 1 mm long, 50-100 µm wide, that blend into a groundmass of aphanitic or glassy plagioclase, with small (~50 µm) opaque phases scattered throughout. There are a few scattered phenocrysts of larger, more intact pyroxene crystals, up to 500 µm in diameter. It has several cracks running through the sample.

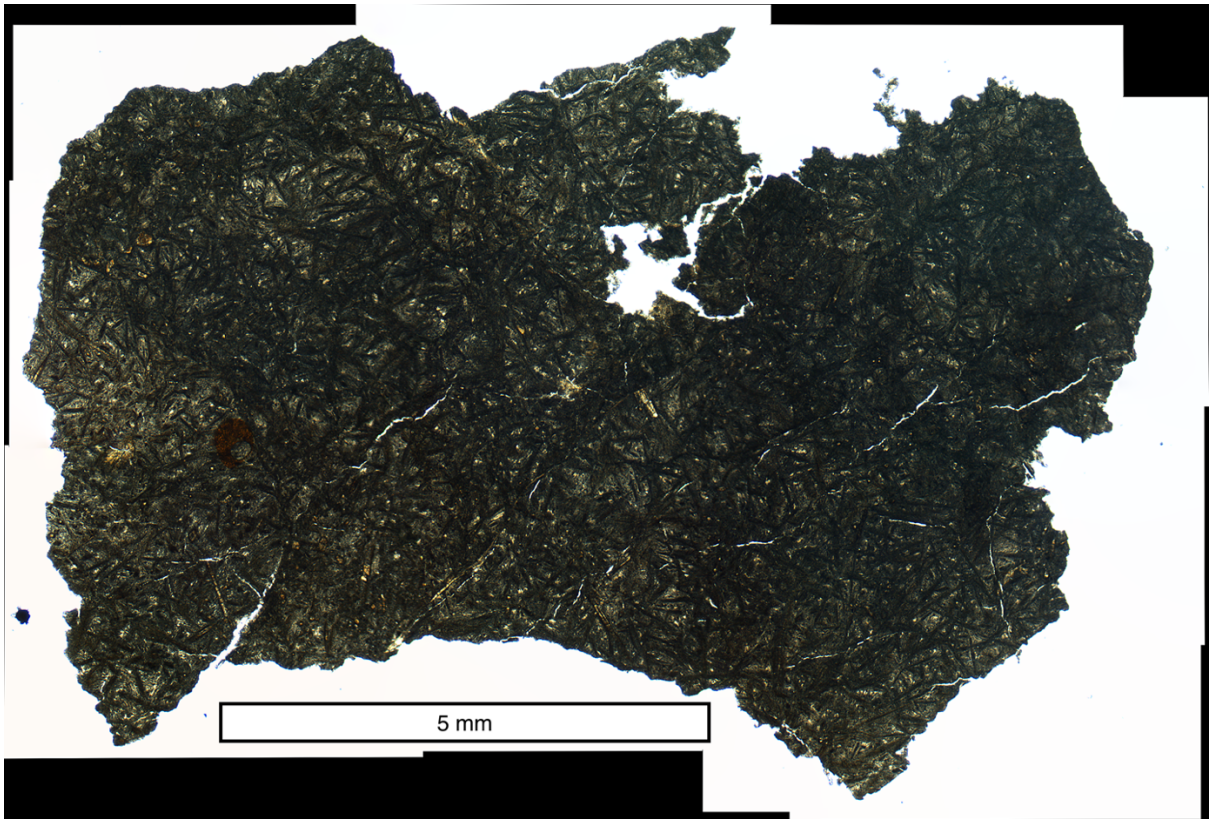

Figure 3. Plane polarized light image of ALHA 81001.

Bates Nunataks 00300 is fine- to medium-grained with a granoblastic texture, and relict subophitic texture (Figure 4). Grain size varies from 50 µm to 600 µm, with an average grain

size of ~200 µm. There are light brown and darker brown pyroxenes, and the elongate plagioclase grains show internal twinning under cross-polarized light but appear to be growing together or maskelynitized under plain polarized light, enclosing some pyroxenes. Some pyroxenes have a striated, exsolution texture. Small opaques (~50 µm) are scattered throughout, and most pyroxenes and some plagioclase grains have tiny inclusions, ~5 µm. Fusion crust is present on this sample.

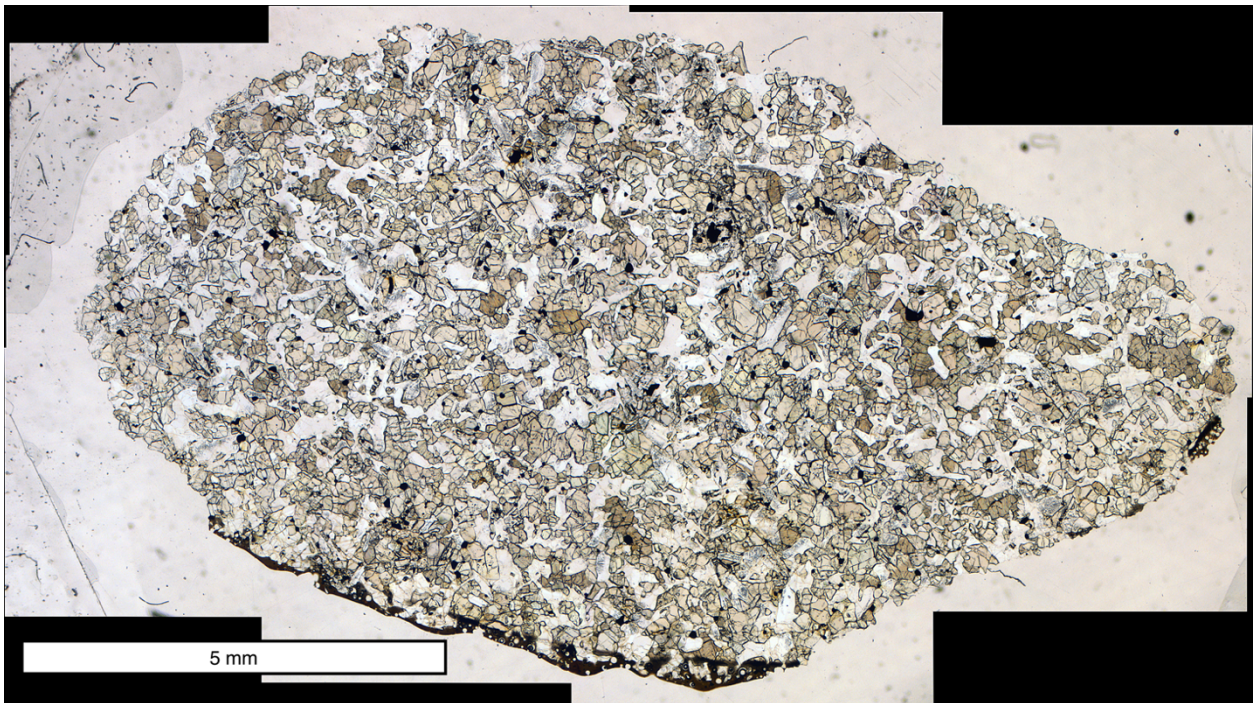

Figure 4. Plane polarized light image of BTN 00300. Note the fusion crust in the bottom portion of the section.

Cumulus Hills 04049 is a relatively coarse-grained rock with a gabbroic, subophitic texture composed of plagioclase and pyroxene, with an average grain size of 1-2 mm (Figure 5). Both minerals show significant shock-darkening throughout the sample. There is a very fine-grained, discolored area of mesostasis in the middle of the section. Few opaque minerals are present, except in the mesostasis area, where they are much more prevalent, but in very small (<100 μm) grains.

Figure 5. Plane polarized light image of CMS 04049. Note yellow discoloration in the center of the image.

Elephant Moraine 90020 has two distinct and separate lithologies (Figure 6). One has a medium-grained texture with larger pyroxenes (~300 μm), and smaller (~100 μm), granulitic plagioclase and lies to the left of the image in Fig. 6. This lithology appears to have much more pyroxene than plagioclase, and has many small (<100 μm) opaques scattered throughout. The other lithology is a fine-grained granoblastic to subophitic texture, with lath-shaped plagioclase

grains intergrowing around pyroxenes. The average grain size is ~250 µm. Pyroxenes in both lithologies show a variety of colors, from dark brown to light brown, and many have a striated exsolution texture. Fusion crust is present on this sample.

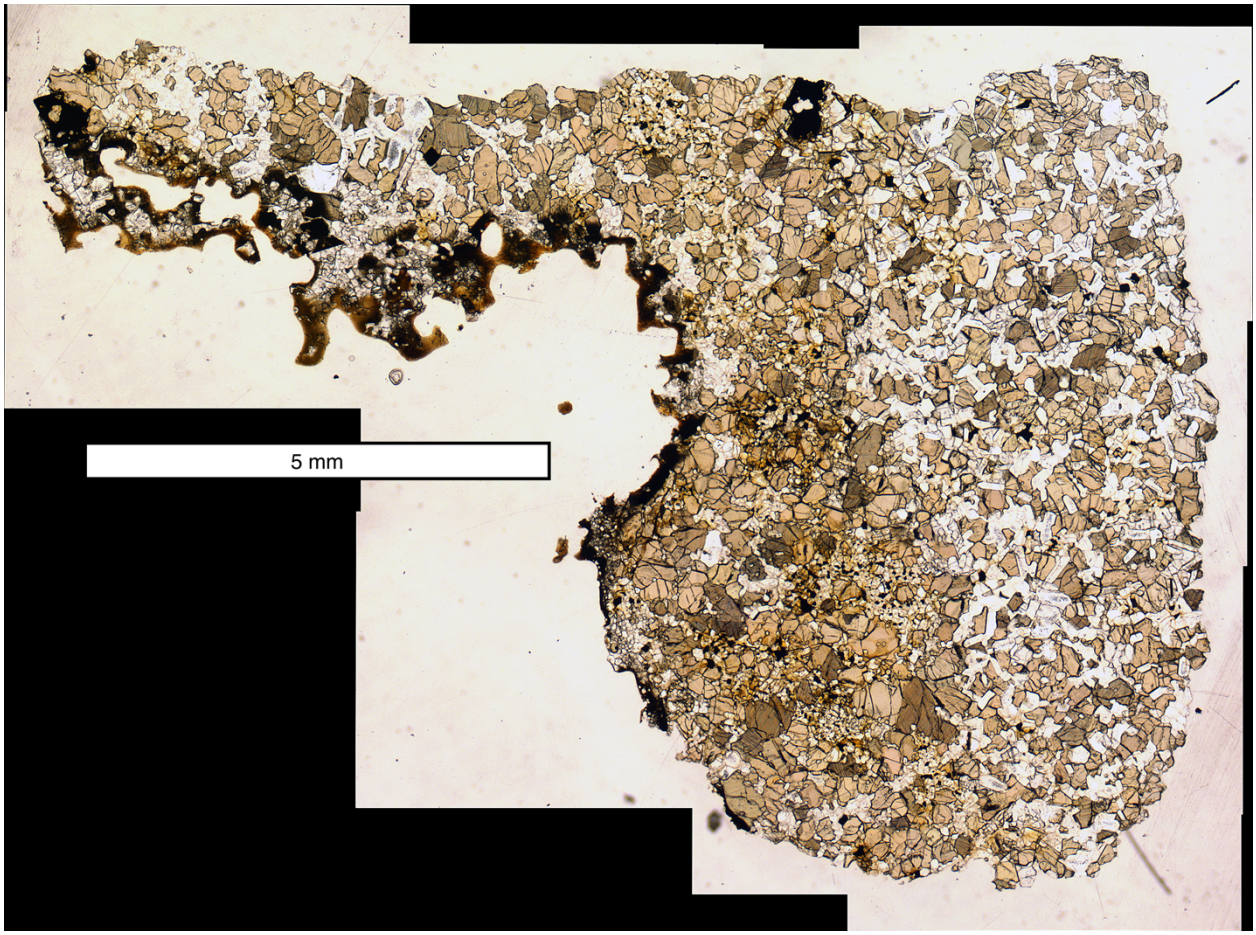

Figure 6. Plane polarized light image of EET 90020. Note the fusion crust on the left-hand edge of the section and the strong lithological variation running up the center of the image.

Graves Nunataks 98098 is fine- to medium-grained with a granular, granoblastic texture, with relict subophitic texture, and some areas with a granulitic texture (Figure 7). The grain size varies from 50 µm to 1 mm, with an average size of ~250 µm. Both light brown and darker brown pyroxenes are present, and many show a striated exsolution texture. Most

plagioclase grains, and a few pyroxene grains have many tiny (~5 μm) inclusions. Small, <100 μm, opaques are present in a few mm-sized clusters across the sample.

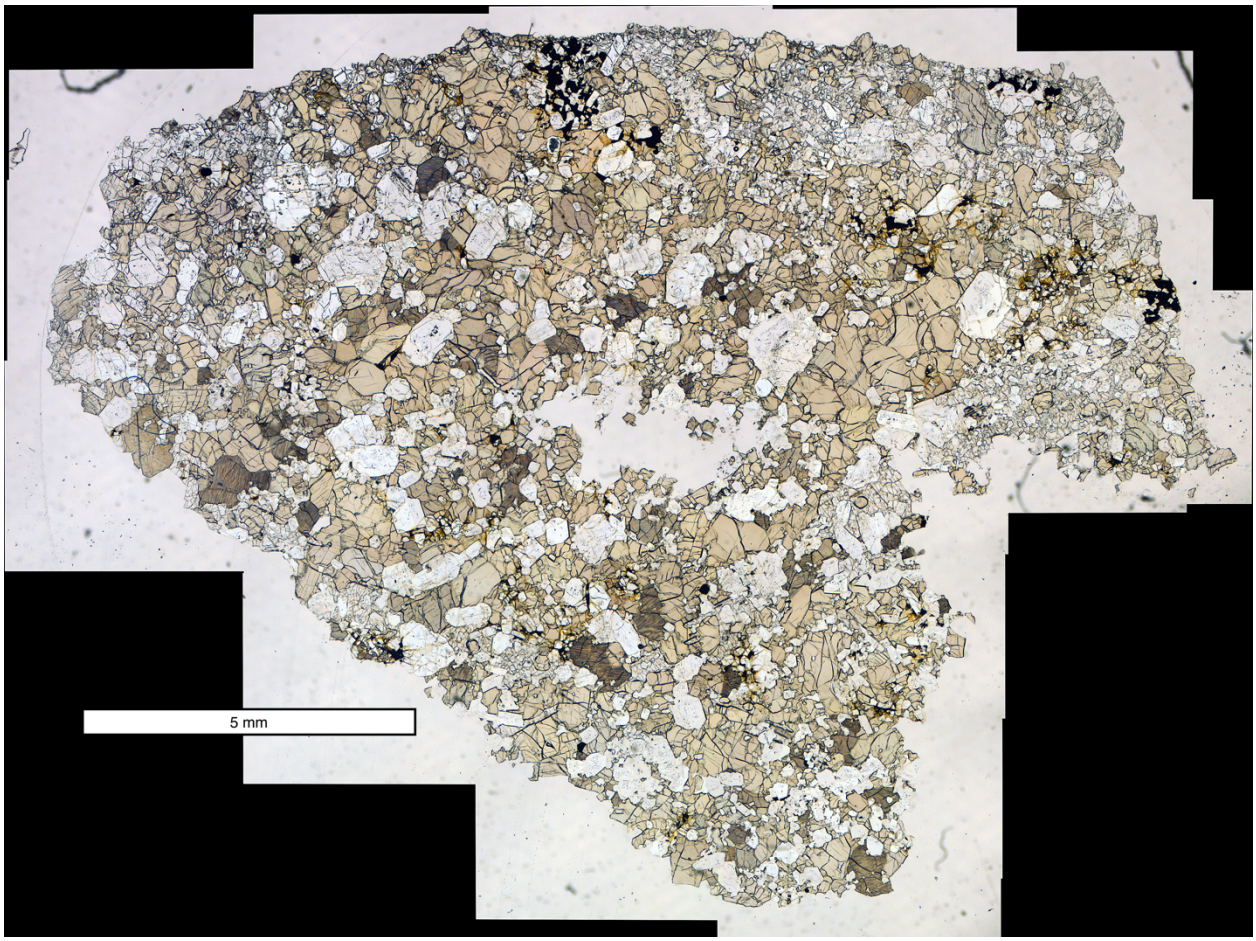

Figure 7. Plane polarized light image of GRA 98098. Note void in middle of sample, and possible lithological variation in the top most portion of the image.

Lewis Cliff 85305 is fine-grained, with a granular, granoblastic texture, with relict subophitic texture (Figure 8). The grain size varies from 50 μm to 500 μm, with an average grain size of about 200 μm. Both light and dark pyroxenes are present, and many show a striated exsolution texture. The plagioclase grains are elongate and show clear internal twinning under cross-polarized light but appear to be growing together or maskelynitized under plain polarized light, enclosing some pyroxenes. There is a very fine-grained area of mesostasis running

through the middle of the sample, and shock-darkening effects are present in both pyroxene and plagioclase. Fusion crust is present on this sample.

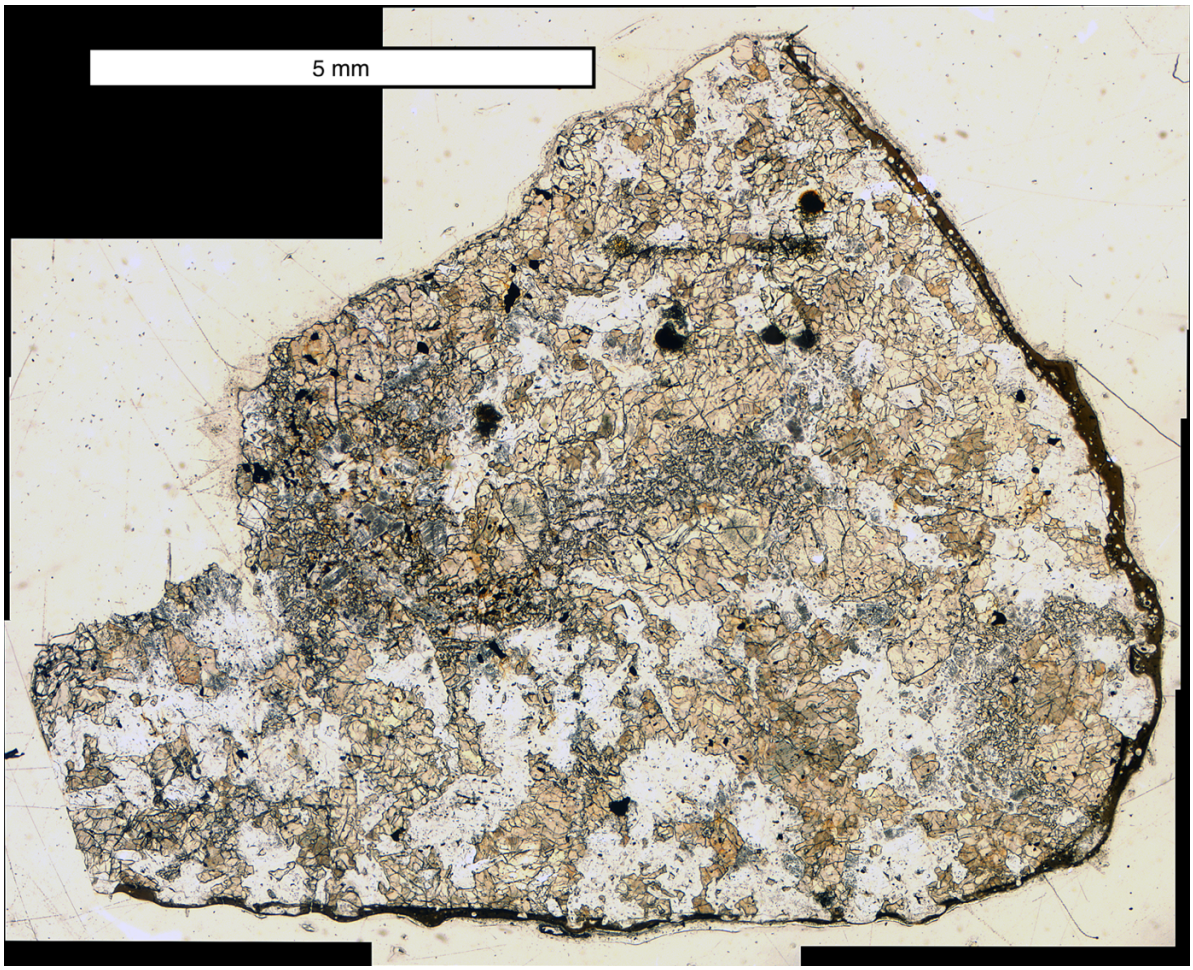

Figure 8. Plane polarized light image of LEW 85305. Note the fusion crust surrounding two sides of the section.

Northwest Africa 1000 is coarse-grained, with a unique acicular texture, with no organized orientation or foliation (Figure 9). It has orange pyroxene grains with an average grain size of about 300 µm, with many elongate pyroxenes up to 10 mm long and 300 µm wide. The plagioclase grains are also elongate, with some up to 3 mm long and 150 µm wide. There are many opaque grains scattered throughout the sample, with an average size of ~100 µm, and some up to 200 µm.

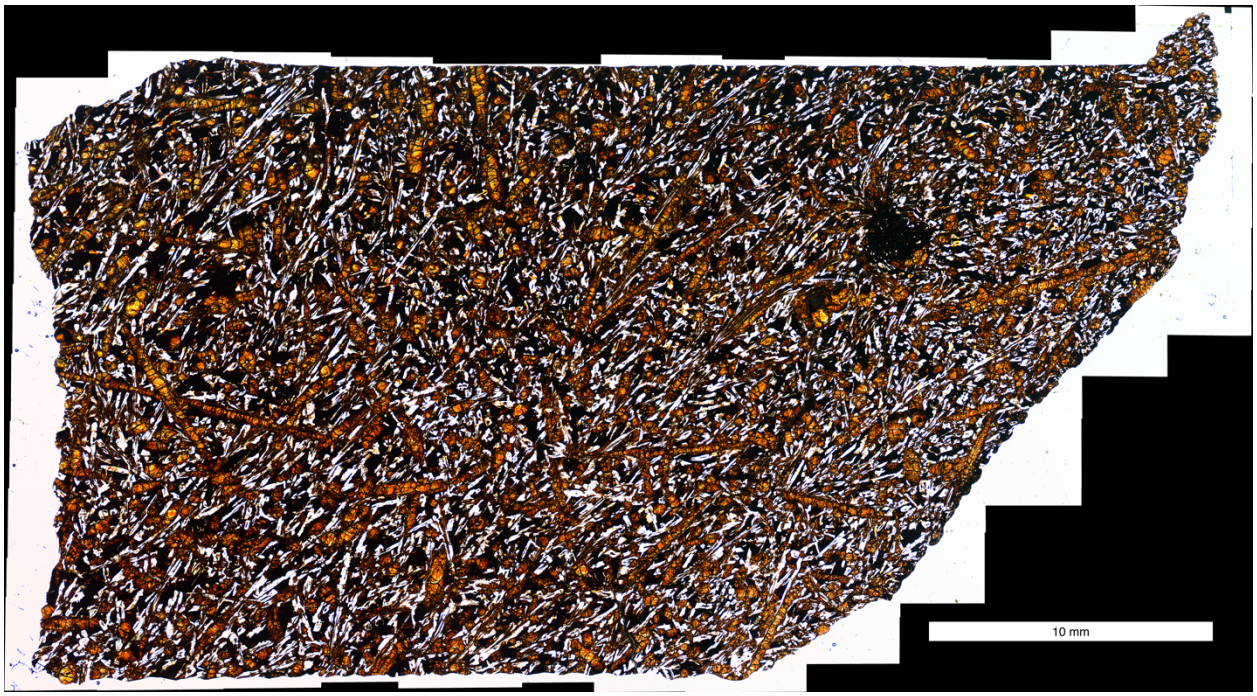

Figure 9. Plane polarized light image of NWA 1000.

Northwest Africa 1923 is coarse-grained, with a granular, granoblastic texture (Figure 10). The average grain size is about 800 µm. Many of the pyroxenes have inclusions or exsolution textures. Very few opaque grains are present, and they are < 50 µm. Note, this sample also has scratches on the bottom of the glass slide, caused during preparation, which cause the large, fuzzy dark streaks across the image.

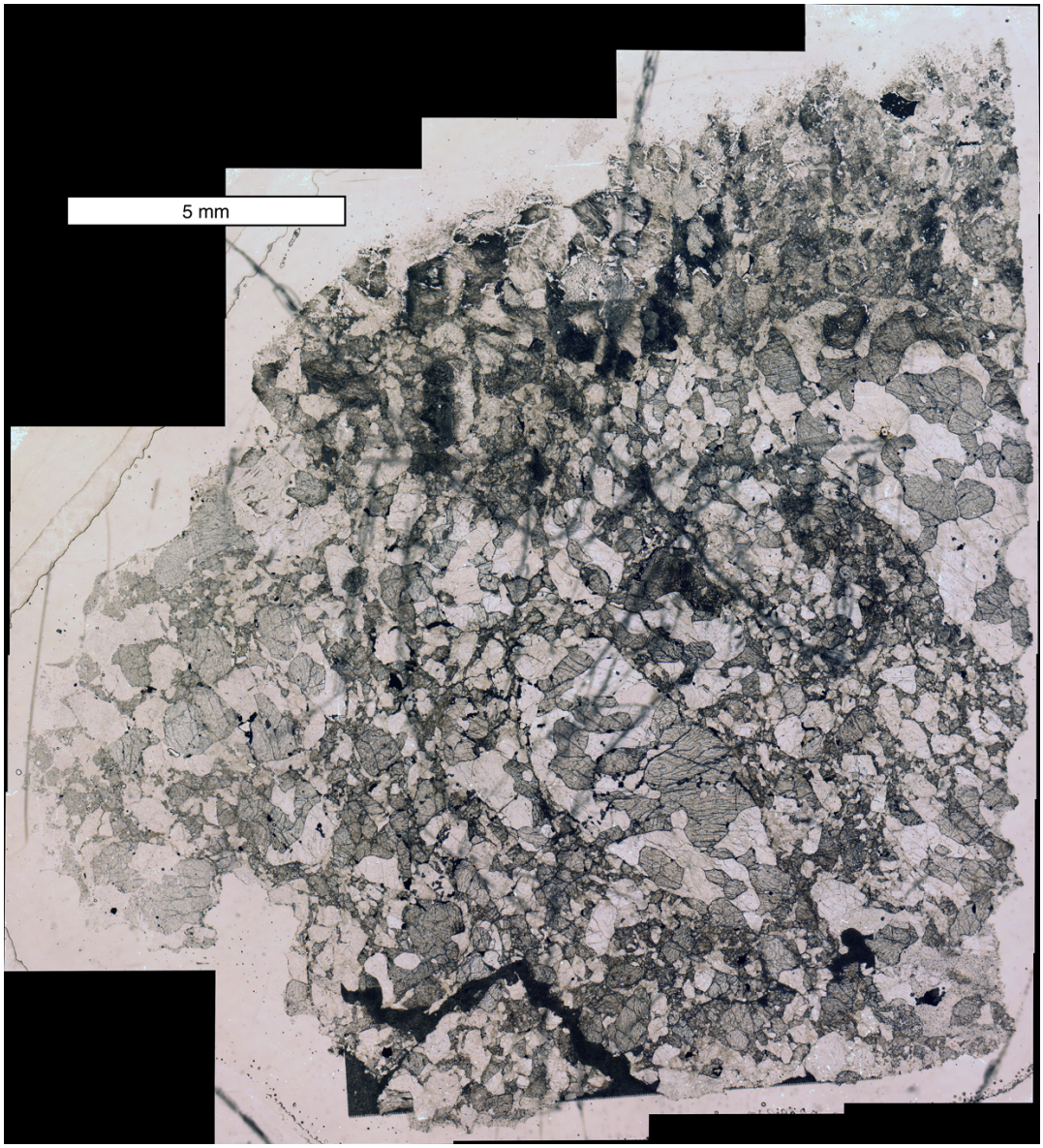

Figure 10. Plane polarized light image of NWA 1923.

Pecora Escarpment 91245 is coarse-grained, with a gabbroic, subophitic texture composed of plagioclase and pyroxene, with an average grain size of 1-2 mm (Figure 11). Both minerals show shock-darkening throughout the sample. There is a very fine-grained area of mesostasis running through the middle of the sample with a cataclasite-like texture. Very few opaque grains are present, and they are < 100 μm.

Figure 11. Plane polarized light image of PCA 91245.

Queen Alexandra Range 97053 is coarse-grained, with a gabbroic, subophitic texture composed of plagioclase and pyroxene, with an average grain size of 500 µm to 1 mm (Figure 12). Pyroxene grains are light brown, and both pyroxene and plagioclase grains show shock-darkening throughout the sample. There is a very fine-grained area of mesostasis running through the middle of the sample with a cataclasite-like texture. Small opaque phases are scattered throughout, with a couple up to 200 µm, but most < 100 µm.

Figure 12. Plane polarized light image of QUE 97053.

3.2. Modal Percentages

The modes measured in this study (Table 2) were plagioclase, pyroxene, and opaques (which included all oxides, sulfides, and metals.) Plagioclase and pyroxene are the dominant phases, and the opaques, while very low in abundance, were easy to distinguish. Other minor phases such as silica-rich phases, apatites, or areas of mesostasis, were not measured, or included in the plagioclase measurement. The grain size in ALHA 81001 was too fine-grained to measure modal percentages.

Table 2. Chart of measured modal abundances from this study

	Plag	Pyx	Opaque
BTN 00300	24%	74%	3%
CMS 04049	44%	54%	3%
EET 90020	22%	72%	4%
GRA 98098	28%	69%	3%
LEW 85305	31%	67%	2%
NWA 1000	23%	75%	1%
NWA 1923	22%	75%	3%
PCA 91245	41%	59%	0%
QUE 97053	35%	65%	1%

3.3. Major Element Abundances

The major elements measured in this study were silicon, calcium, and iron, and data is shown in Table 3. As mentioned in section 2.2, all data were corrected to silicon, with values taken from Mayne et al. (2009) and Dhaliwal et al. (in review). Silicon data for NWA 1000 and NWA 1923 was collected via electron microprobe by Kim Tait. Reported Ca and Fe data is LA-ICP-MS data from this study. Since ALHA 81001 ended up being too fine-grained to measure the different phases separately, those data are reported later as bulk rock concentrations, similar to the reported data for the fusion crust.

Table 3. Major Element Abundances – wt. % oxide. Unless marked, LA-ICP-MS data from this study. (1) from Mayne et al. (2009). (2) from Dhaliwal et al. (in review). (3) new EMP data

	Average Pyroxene			Average Plagioclase		
	SiO	CaO	FeO	SiO	CaO	FeO
BTN 00300	49.8 [1]	6.2	28.4	45.3 [1]	16.7	0.2
CMS 04049	49.1 [2]	4.0	33.0	47.0 [2]	17.6	1.2
EET 90020	48.4 [1]	6.4	28.7	45.8 [1]	16.7	0.4
GRA 98098	49.7 [1]	6.1	26.8	47.2 [1]	16.9	0.3
LEW 85305	50.0 [1]	10.7	26.1	46.4 [1]	14.1	0.1
NWA 1000	52.8 [3]	2.1	21.1	48.0 [3]	15.8	0.8
NWA 1923	52.4 [3]	3.0	22.0	43.8 [3]	16.8	0.1
PCA 91245	48.6 [2]	6.4	31.9	44.8 [2]	14.3	0.6
QUE 97053	49.8 [1]	3.7	29.8	47.2 [1]	17.2	0.9

3.3.1 Pyroxene Grains

Overall, the pyroxene grains measured were broadly similar across the different samples, with average silicon values of 50.1 ± 1.5 weight percent. Iron values were also broadly similar, with average values of 27.5 ± 4.0 weight percent. The calcium values were more variable, ranging from 2.1 to 10.7, with an average of 5.4 weight percent.

3.3.2 Plagioclase Grains

The plagioclase grains measured were also broadly similar across all nine samples, with average silicon values of 46.2 ± 1.4 weight percent. Calcium values were also similar, with average values of 16.2 ± 1.3 weight percent. The iron values were predictably low, and more variable, ranging from 0.1 to 1.2 weight percent, with an average of 0.5.

3.3.3 Fusion crust and ALHA 81001

Fusion crust measurements were taken from BTN 00300, EET 90020, and LEW 85305. The complete data from ALHA 81001 are also included in this section since it turned out to be too fine-grained to measure distinct phases. Like the fusion crust, these measurements represent the bulk rock. The bulk rock data in Table 4 is from Dhaliwal et al. (in review) and illustrates the similarity between fusion crust and bulk rock measurements.

Table 4. Major Element Abundances for fusion crust and ALHA 81001 – wt. % oxide. Bulk rock data from Dhaliwal et al. (in review).

	Measured Values			Bulk Rock		
	SiO	CaO	FeO	SiO	CaO	FeO
ALHA 81001	56.6	9.9	28.0	51.3	9.1	17.5
stdev		*5.4*	*2.2*			
BTN 00300	49.6	10.6	19.3	49.6	10.1	17.8
stdev		*0.9*	*3.5*			
EET 90020	48.3	11.3	22.0	48.3	10.1	19.2
stdev		*1.4*	*5.7*			
LEW 85305	46.3	10.2	17.6	46.3	9.3	22.0
stdev		*1.5*	*4.6*			

3.4. Trace Element Abundances

The following incompatible trace element diagrams are shown with the typical order of elements (more incompatible elements on the left side of the graph, and less incompatible on the right side) with a few exceptions. Lead was moved farther to the left side of the diagram, and Zn and K were added on the left side as well, so that the MVE's are shown together on the left-most side of the diagrams.

3.4.1 Pyroxene Grains

Trace element data for BTN 00300 reveals two distinct sets of pyroxene grains, with little variability within each set (Figure 13). The general shape of both trends is a positive slope, where they have lower abundances in the more incompatible elements (leftmost side of figure), and higher abundances of the less incompatible elements (rightmost side of the figure). Compared to the general pattern, both trends show lower abundances of Cs, Zn, K, Rb, Pb, Ba, Sr, and Eu, and Li is slightly lower. The trend with higher abundances overall is also higher in Ca, but lower in Fe and Nb. The rare earth element (REE) data for BTN 00300 shows the same two sets of pyroxene grains, with little variability within each set, varying by less than half an order of magnitude. The general shape of both trends is a positive slope, with an average La/Yb ratio of 0.07. Both trends show relative depletions in Eu, with an average Eu* value of 0.04. Eu*, or the Eu anomaly, is a measure of difference from the REE trend, as calculated by: $[\mathrm{Eu}]/\sqrt{[\mathrm{Sm}][\mathrm{Gd}]}$.

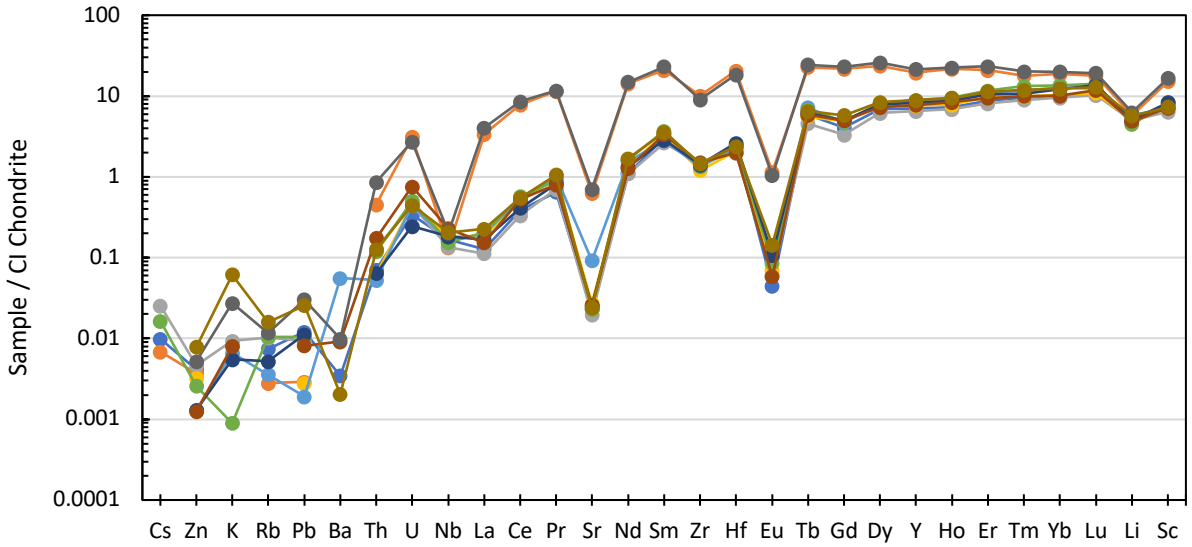

Figure 13. Incompatible trace element diagram for BTN 00300 pyroxene grains. CI chondrite normalization from McDonough and Sun (1995).

The trace element data for CMS 04049 pyroxene grains varies by about half an order of magnitude with slightly more variability toward the more incompatible side of the diagram (Figure 14). The general pattern is a positive slope, where they have lower abundances in the more incompatible elements, and higher abundances of the less incompatible elements. Compared to the general pattern, there are lower abundances of Cs, Zn, K, Rb, Pb, Ba, Sr, and Eu, and Li is slightly lower as well. Th and U are more abundant when compared to the general trend. One grain has higher abundances of many elements, up to about an order of magnitude higher. Another grain falls within the general trend for most elements but does not show the depletions in Sr and Eu, and is higher in Ba than the general trend. The rare earth element data for CMS 04049 pyroxene grains varies by about half an order of magnitude, with one grain more enriched in all elements. The general pattern is a positive slope, with an average La/Yb ratio of 0.04. There is a strong relative depletion in Eu in all grains measured but one, which shows a slight enrichment. The average Eu* value is 0.14.

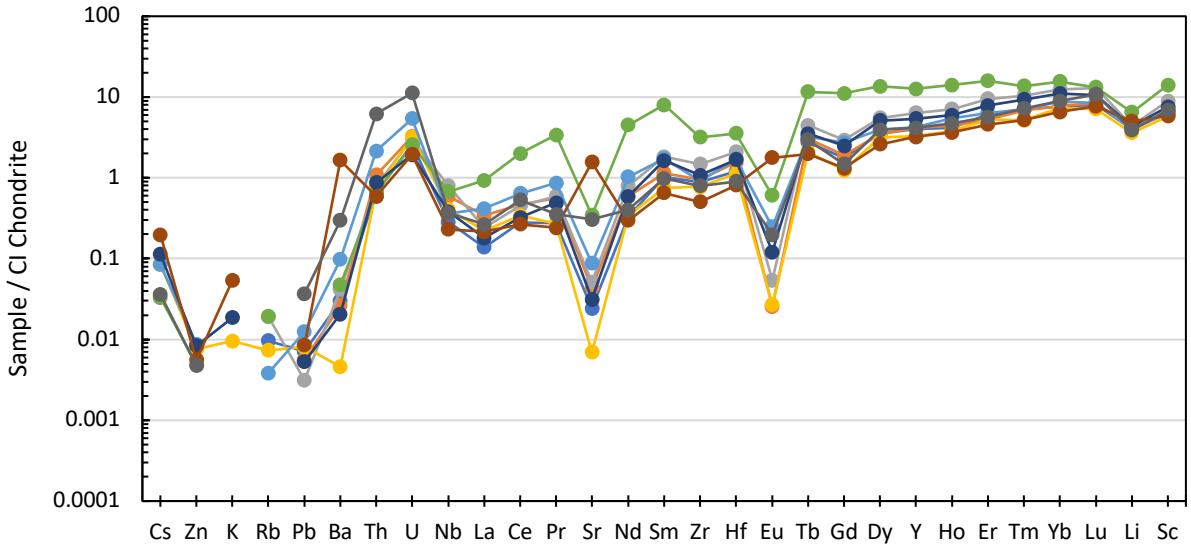

Figure 14. Incompatible trace element diagram for CMS 04049 pyroxene grains. CI chondrite normalization from McDonough and Sun (1995).

The trace element data for EET 90020 pyroxene grains shows little variability across all elements, varying by at most a half an order of magnitude on the more incompatible side of the diagram (Figure 15). The general pattern is a positive slope, where they have lower abundances in the more incompatible elements, and higher abundances of the less incompatible elements. Compared to the general pattern, there are lower abundances of Cs, Zn, K, Rb, Pb, Ba, Sr, and Eu, and Li is slightly lower. One grain has a higher abundance of K than the rest of the grains. The rare earth element data for EET 90020 pyroxene grains varies by less than half an order of magnitude. The general pattern is a positive slope, with an average La/Yb ratio of 0.06. There is a strong relative depletion in Eu, with an average Eu* value of 0.06.

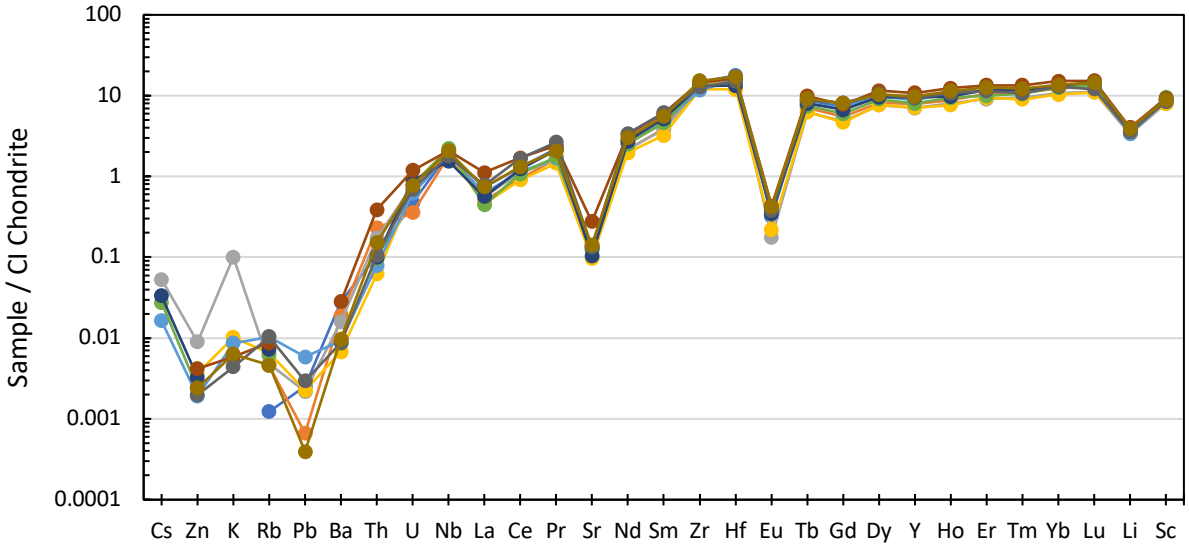

Figure 15. Incompatible trace element diagram for EET 90020 pyroxene grains. CI chondrite normalization from McDonough and Sun (1995).

The trace element data for GRA 98098 pyroxene grains varies by up to an order of magnitude with slightly less variability toward the less incompatible side of the diagram (Figure 16). The general pattern is a positive slope, where they have lower abundances in the more incompatible elements, and higher abundances of the less incompatible elements. Compared to the general pattern, there are lower abundances of Cs, Zn, K, Rb, Pb, Ba, Sr, and Eu, and Li and Sc are slightly lower. Uranium appear enriched relative to the general trend. The rare earth element data for GRA 98098 pyroxene grains varies by less than one order of magnitude on the more incompatible side of the diagram and less than one half order of magnitude on the less incompatible side. The general pattern is a positive slope, with an average La/Yb ratio of 0.06. There is a strong relative depletion in Eu, with an average Eu* value of 0.05.

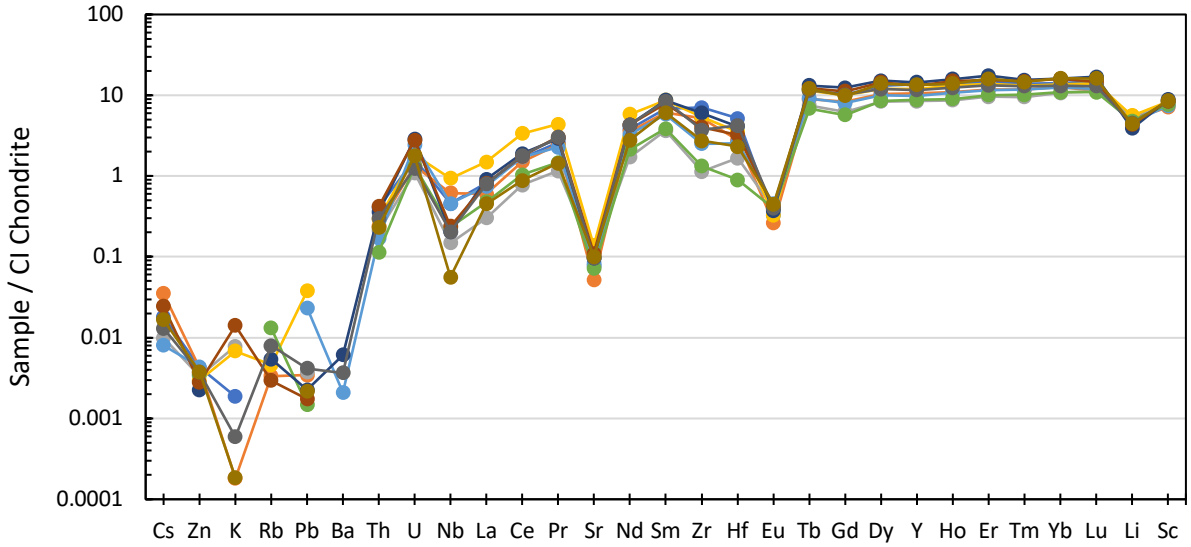

Figure 16. Incompatible trace element diagram for GRA 98098 pyroxene grains. CI chondrite normalization from McDonough and Sun (1995).

The trace element data for LEW 85305 pyroxene grains varies by up to an order of magnitude on the more incompatible side of the diagram and half an order of magnitude on the less incompatible side (Figure 17). The general pattern is a positive slope, where they have lower abundances in the more incompatible elements, and higher abundances of the less incompatible elements. Compared to the general pattern, there are lower abundances of Cs, Zn, K, Rb, Pb, Ba, Sr, Eu, and Li. The rare earth element data for LEW 85305 pyroxene grains varies by a little over an order of magnitude on the more incompatible side of the diagram and less than one half order of magnitude on the less incompatible side. The general pattern is a positive slope, with an average La/Yb ratio of 0.13. There is a strong relative depletion in Eu, with an average Eu* value of 0.06.

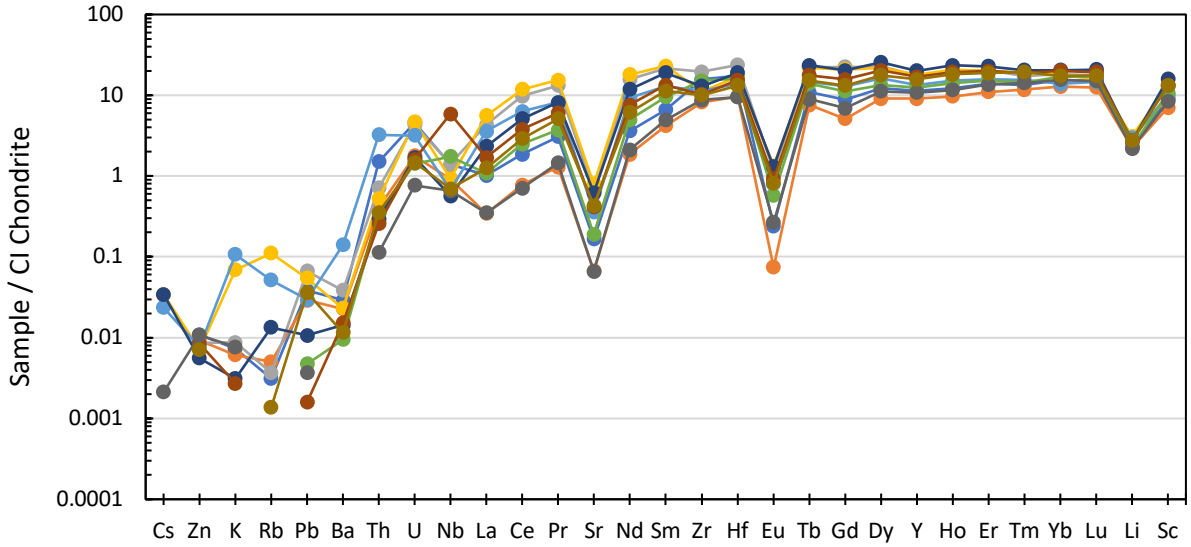

Figure 17. Incompatible trace element diagram for LEW 85305 pyroxene grains. CI chondrite normalization from McDonough and Sun (1995).

The trace element data for NWA 1000 pyroxene grains varies by about half an order of magnitude with less variability toward the less incompatible trace element side of the diagram (Figure 18). The general pattern is a positive slope, where they have lower abundances in the more incompatible elements, and higher abundances of the less incompatible elements. Compared to the general pattern, there are lower abundances of Cs, Zn, Rb, Pb, Zr, Hf, and Eu. Barium, Th, U, and Li have higher abundances than the general trend. Potassium also has a lower abundance than the general trend, but is higher than the other MVE's. The rare earth element data for NWA 1000 pyroxene grains varies by less than an order of magnitude on the more incompatible side, and less than half an order of magnitude on the less incompatible side. The general pattern is a positive slope, with an average La/Yb ratio of 0.23. All grains show a relative depletion in Eu, with an average Eu* value of 0.16.

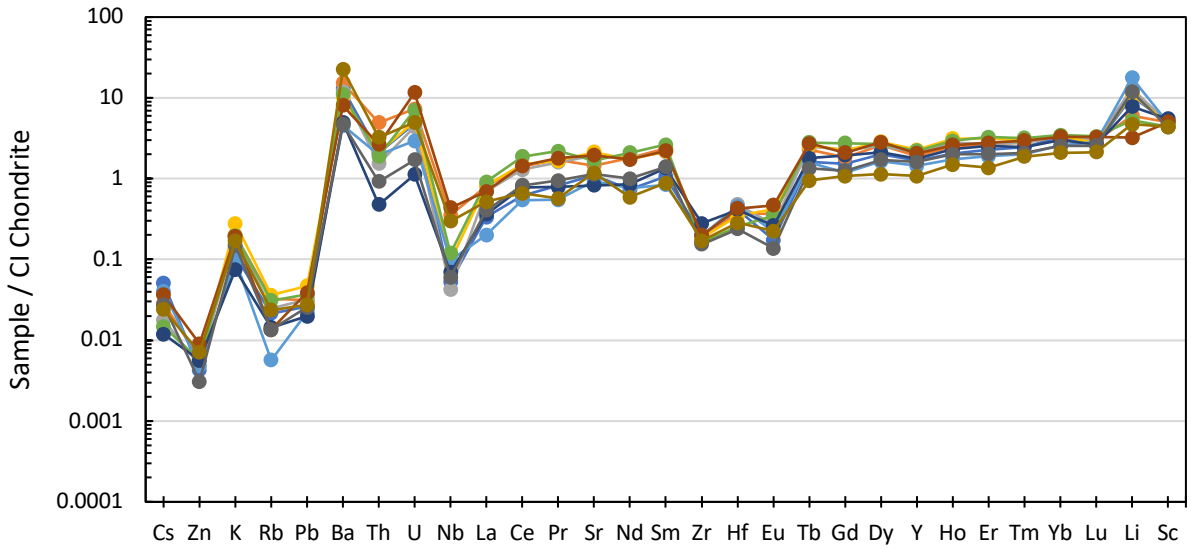

Figure 18. Incompatible trace element diagram for NWA 1000 pyroxene grains. CI chondrite normalization from McDonough and Sun (1995).

The trace element data for NWA 1923 pyroxene grains varies by about an order of magnitude across all elements, although Li an Sc show very little variance (Figure 19). The general pattern is a slight positive slope, where they have lower abundances in the more incompatible elements, and higher abundances of the less incompatible elements. Almost all of the elements have very low abundances compared to the other samples studied. Uranium, Li, and Sc have higher abundances relative to the general trend of this sample. The rare earth element data for NWA 1923 pyroxene grains varies by about an order of magnitude. The general pattern is a positive slope, with an average La/Yb ratio of 0.23. There is a relative depletion in Eu in most grains, with an average Eu* value of 0.31. All grains are depleted compared to chondritic abundances as well as the other samples measured.

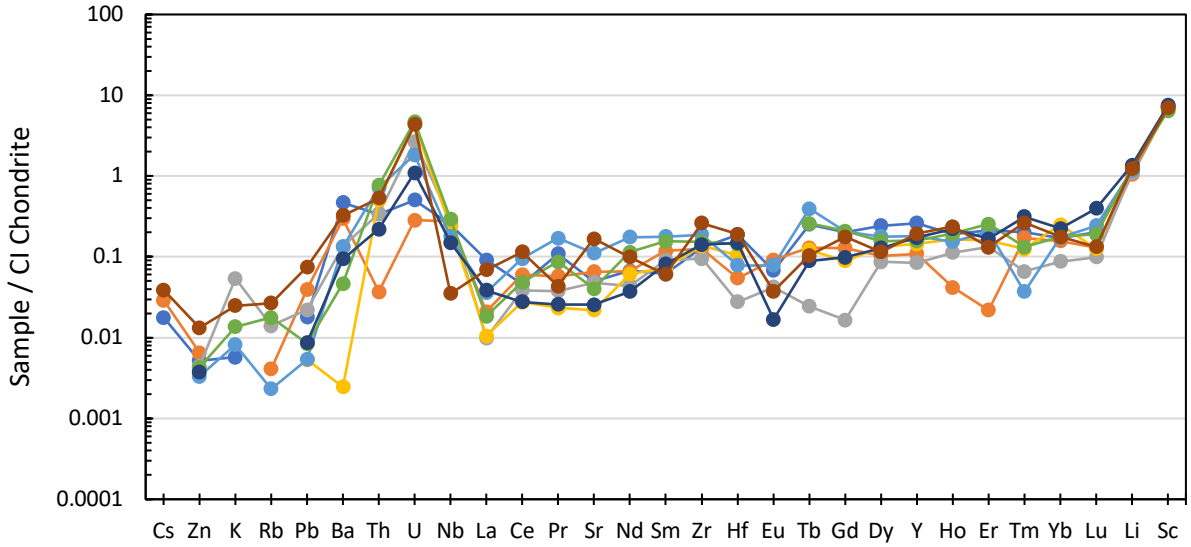

Figure 19. Incompatible trace element diagram for NWA 1923 pyroxene grains. CI chondrite normalization from McDonough and Sun (1995).

The trace element data for PCA 92145 pyroxene grains varies by a little over an order of magnitude on the more incompatible trace element side of the diagram and half an order of magnitude on the less incompatible side (Figure 20). The general pattern is a positive slope, where they have lower abundances in the more incompatible elements, and higher abundances of the less incompatible elements. Compared to the general pattern, there are low abundances of Cs, Zn, K, Rb, Pb, Sr, and Eu, and Li is slightly lower. Barium, Th, and U have higher abundances than the general trend. The rare earth element data for PCA 92145 pyroxene grains varies by about an order of magnitude across all elements. The general pattern is a positive slope, with an average La/Yb value of 0.11. All grains show a relative depletion in Eu, with an average Eu* value of 0.17.

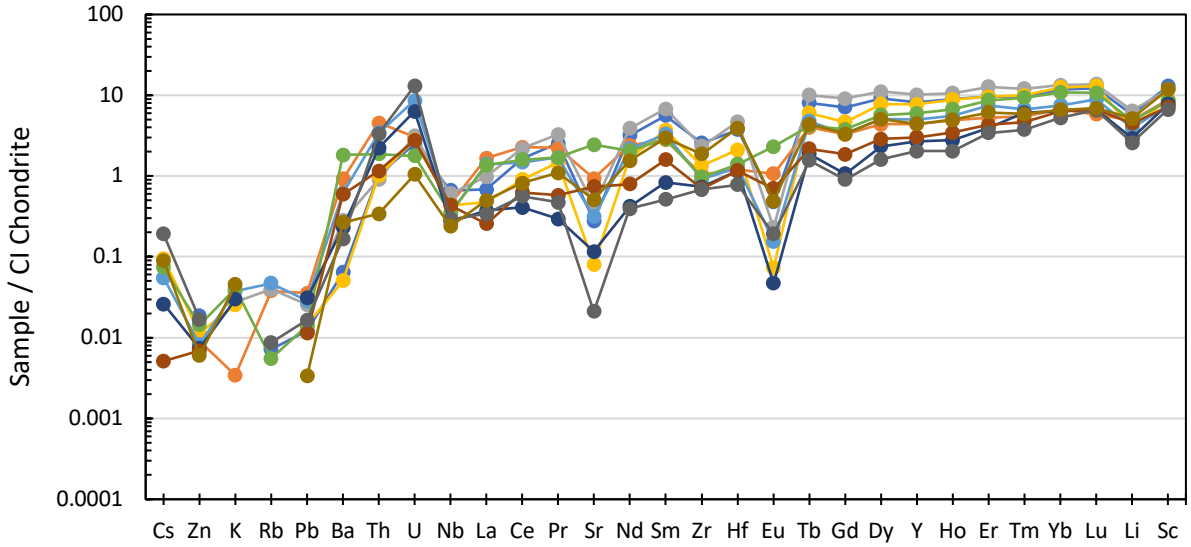

Figure 20. Incompatible trace element diagram for PCA 92145 pyroxene grains. CI chondrite normalization from McDonough and Sun (1995).

The trace element data for QUE 97053 pyroxene grains varies by about one and a half orders of magnitude on the more incompatible trace element side of the diagram and one order of magnitude on the less incompatible side (Figure 21). The general pattern is a positive slope, where they have lower abundances in the more incompatible elements, and higher abundances of the less incompatible elements. Compared to the general pattern, there are lower abundances of Cs, Zn, K, Rb, Pb, Ba, Sr, and Eu, and Li is slightly lower. U has a higher abundance relative to the general trend. The rare earth element data for QUE 97053 pyroxene grains varies by about one and a half orders of magnitude on the more incompatible side of the diagram and about one order of magnitude on the less incompatible side. The general pattern is a positive slope, with an average La/Yb ratio of 0.07. All grains show a relative depletion in Eu, with an average Eu* value of 0.12.

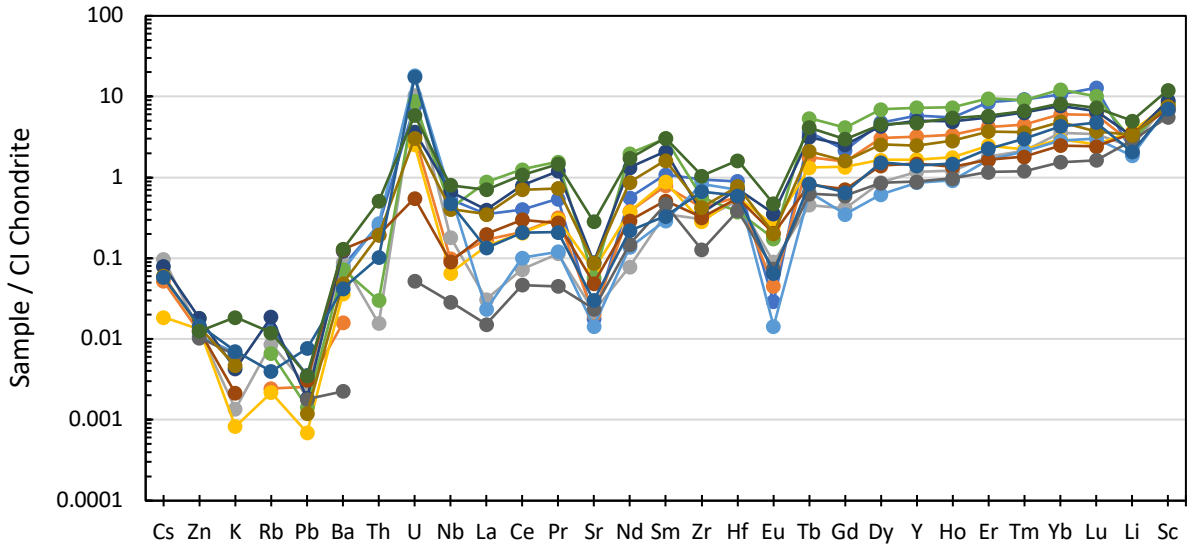

Figure 21. Incompatible trace element diagram for QUE 97053 pyroxene grains. CI chondrite normalization from McDonough and Sun (1995).

In order to directly compare samples, the average of all pyroxene grains for each sample is given in Figure 22. Overall, the eucrites have very similar patterns of trace elements but about an order of magnitude variation in their absolute abundances. NWA 1923 is anomalous compared to the other samples, being one to two orders of magnitude lower in abundances in most elements besides the MVE's, and it does not show a relative depletion in Sr. NWA 1000 is also a little different, having a flatter slope, higher abundances of Zn, K, and Li, and no relative depletion in Sr. All samples show the same general pattern of a positive slope, where they have lower abundances in the more incompatible elements, and higher abundances of the less incompatible elements. They all have lower abundances of Cs, Zn, K, Rb, Pb, and Eu, and most also show depletions in Ba and Sr, and a slight depletion in Li.

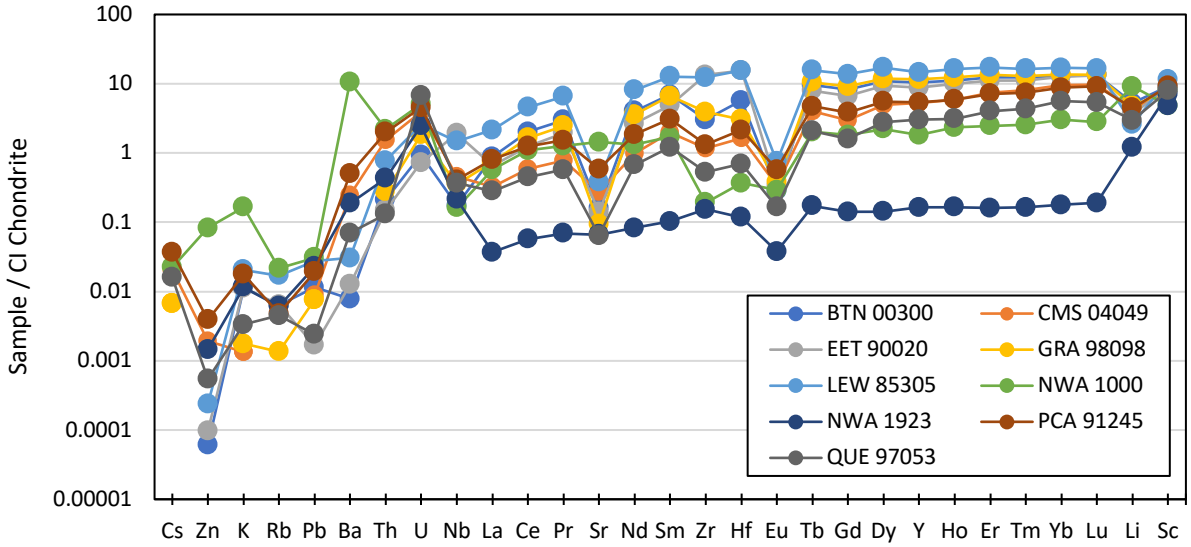

Figure 22. Incompatible trace element diagram of average pyroxene grain composition for each eucrite. To see range of values for each eucrite, see individual diagrams above. CI chondrite normalization from McDonough and Sun (1995).

For the rare earth elements (Figure 23), the eucrites vary by about an order of magnitude, except for NWA 1923 which has lower abundances than the other samples by about one and a half orders of magnitude. All samples show the same general pattern of a negative slope, with an average La/Yb ratio of 0.11. However, NWA 1000 has a flatter slope than the other eucrites. All eucrites show relative depletions in Eu, with an average Eu* value of 0.12.

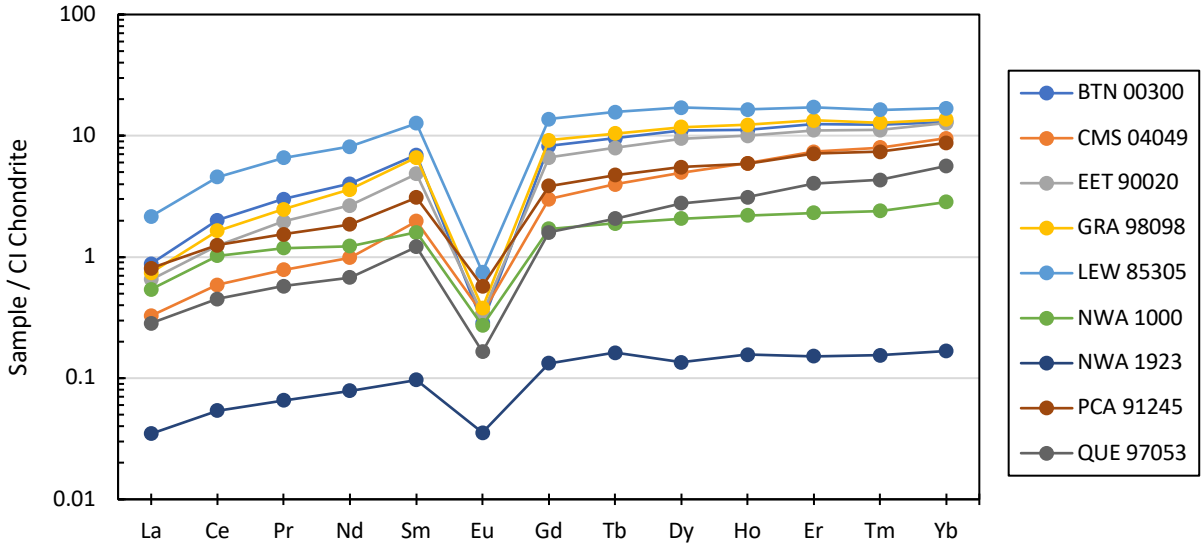

Figure 23. Average pyroxene grain rare earth element diagram. CI chondrite normalization from McDonough and Sun (1995).

3.4.2 Plagioclase Grains

Trace element data for BTN 00300 plagioclase grains varies by about an order of magnitude with more variability in Cs, Zn, Rb, Pb, Th, U, Nb, Zr, and Hf (Figure 24). The general shape is a slightly negative slope, where they have higher abundances in the more incompatible elements, and lower abundances of the less incompatible elements. Compared to the general pattern, most grains have lower abundances of Cs, Zn, Rb, Pb, and higher abundances of Eu, Sr, and Li. There are three grains with very little variance to each other that generally have higher abundances than the rest of the grains, and do not have the higher

abundances of Eu, Sr, and Li. These grains have anomalous K/Ca ratios 6-7 times higher than the other grains (thus throwing off their data correction from raw counts per second) and higher relative abundances of all elements but Ba, Sr, Eu, and Li. Additionally, these grains are not located near the anomalous pyroxene grains found in BTN 00300. The REE data for BTN 00300 also shows the anomalous plagioclase grains, which appear to generally have higher abundances, but do not have a Eu anomaly (average Eu* of 1). The normal REE trend shows a strong Eu enrichment, with an average Eu* value of 23, and an average La/Yb ratio of 34.4. The general shape of both trends is a negative slope.

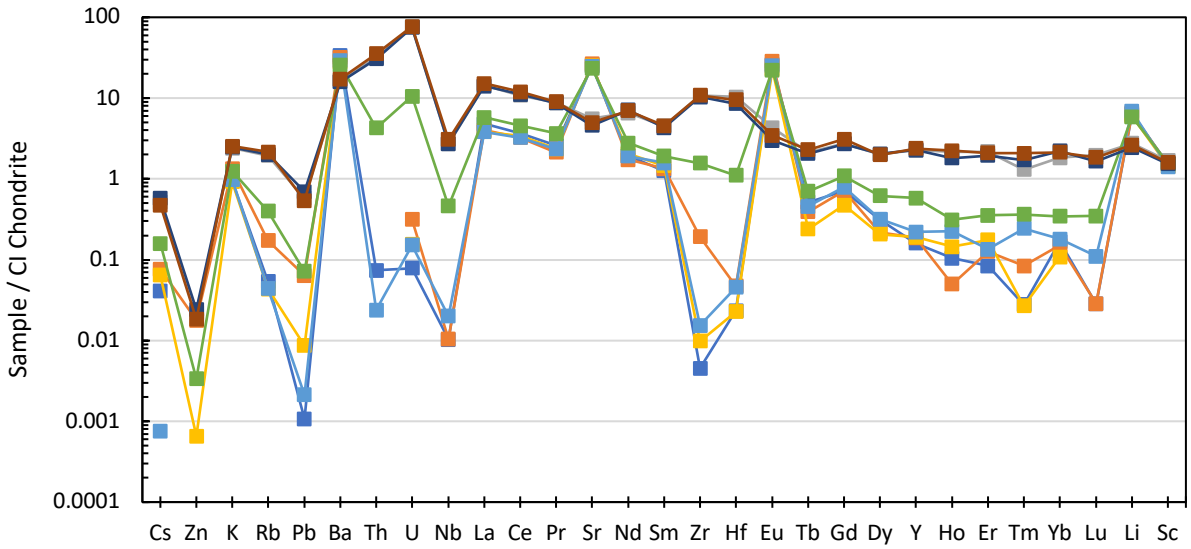

Figure 24. Incompatible trace element diagram for BTN 00300 plagioclase grains. CI chondrite normalization from McDonough and Sun (1995).

The trace element diagram for CMS 04049 plagioclase grains varies by a little over order of magnitude for most elements (Figure 25). Barium, Pr, Sr, Eu, Li, and Sc show very little variance. The general shape is a flat pattern. Compared to the general pattern, there are higher abundances of Ba, Sr, Eu, and Li, and lower abundances of Zn, Pb and Zr. The rare earth element data for CMS 04049 plagioclase grains varies by about an order of magnitude. The general pattern is a negative slope, with an average La/Yb ratio of 6.7. All grains show a strong relative enrichment in Eu, with an average Eu* value of 44.

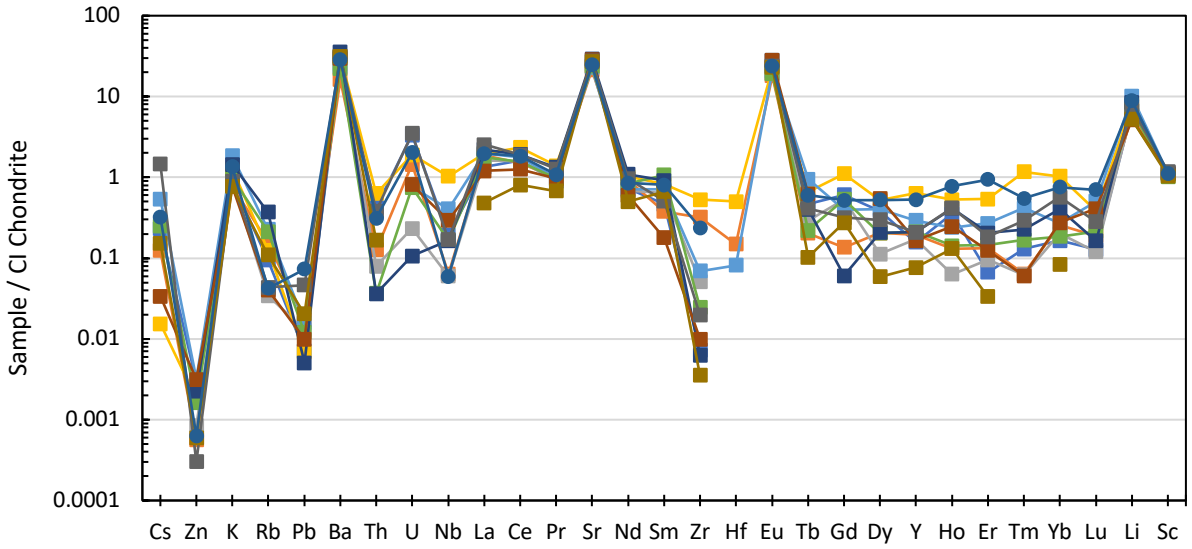

Figure 25. Incompatible trace element diagram for CMS 04049 plagioclase grains. CI chondrite normalization from McDonough and Sun (1995).

Trace element data for EET 90020 plagioclase grains varies by about an order of magnitude with more variation in Th, U, Nb, Zr, and Hf (Figure 26). The general pattern is a negative slope, enriched in the more incompatible elements, and depleted in the less incompatible elements. Compared to the general pattern, there are higher abundances of Ba, Sr, Eu, Li, and Sc, and lower abundances of Cs, Zn, Rb and Pb. The rare earth element data for EET 90020 plagioclase grains shows good agreement across all elements. The general pattern is a negative slope, with an average La/Yb ratio of 32.5. All grains show a strong relative enrichment in Eu, with an average Eu* value of 35.

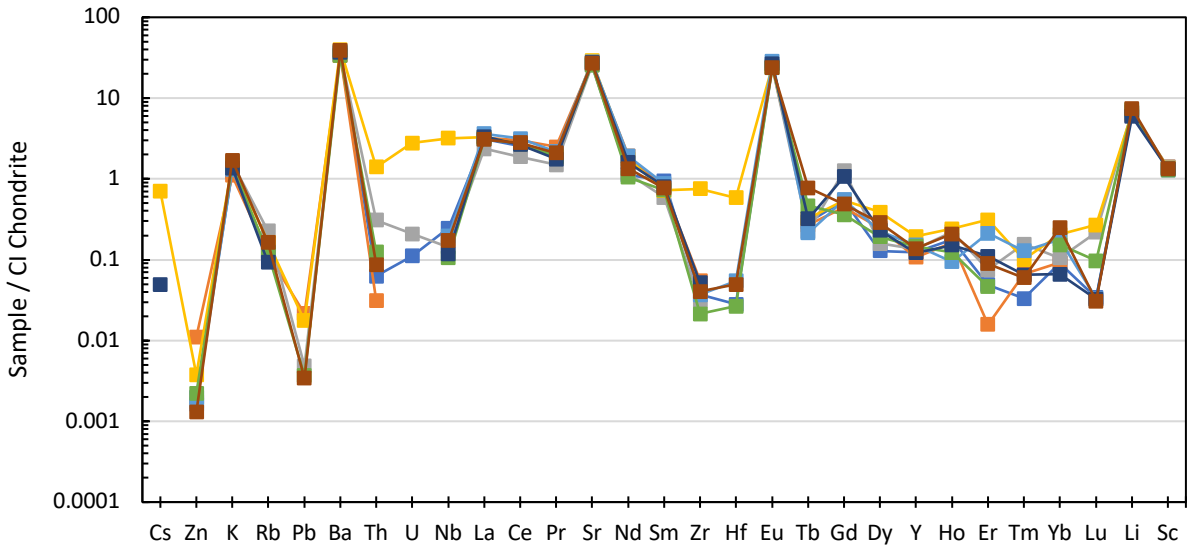

Figure 26. Incompatible trace element diagram for EET 90020 plagioclase grains. CI chondrite normalization from McDonough and Sun (1995).

The trace element diagram for GRA 98098 plagioclase grains shows good agreement across most elements, varying by about an order of magnitude, with more variation in Th, U, Nb, Pb, and Tb. K, Sr, Eu, Li, and Sc are in very strong agreement (Figure 27). The general pattern is a slightly negative slope, where they have higher abundances in the more incompatible elements, and lower abundances of the less incompatible elements. Compared to the general pattern, there are higher abundances of Ba, Sr, Eu, Li, and Sc, and lower abundances of Cs, Zn, Rb, and Pb. The rare earth element data for GRA 98098 plagioclase grains shows good agreement across all elements. The general pattern is a negative slope, with an average La/Yb ratio of 33.7. All grains show a strong relative enrichment in Eu, with an average Eu* value of 20.

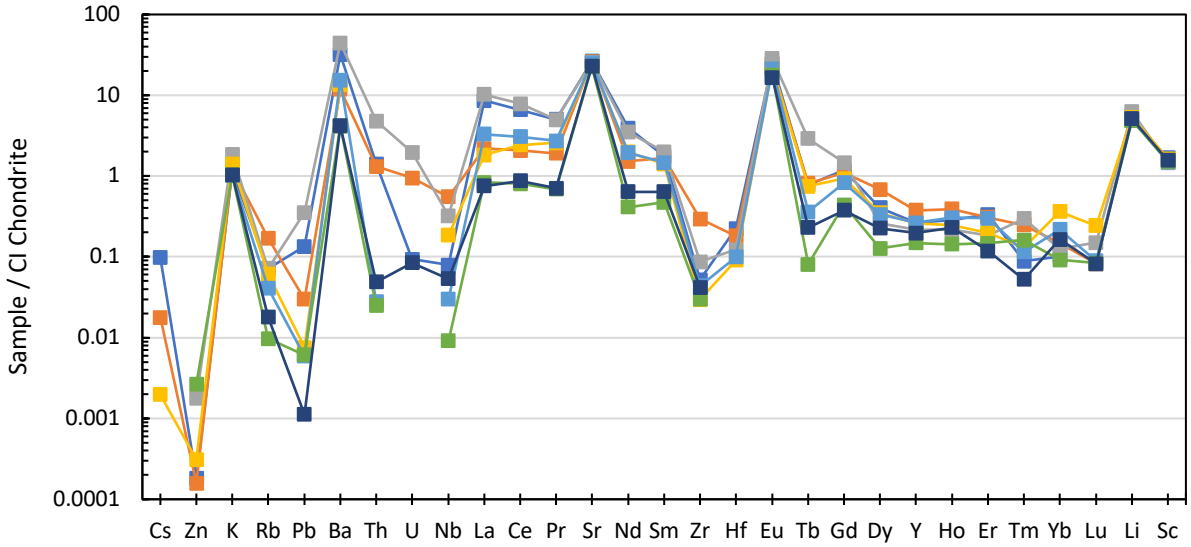

Figure 27. Incompatible trace element diagram for GRA 98098 plagioclase grains. CI chondrite normalization from McDonough and Sun (1995).

The trace element diagram for LEW 85305 varies by about an order of magnitude (Figure 28). The general pattern is a negative slope, where they have higher abundances in the more incompatible elements, and lower abundances of the less incompatible elements. Compared to the general pattern, there are higher abundances of Ba, Sr, Eu, Li, and Sc, and lower abundances of Cs, Zn, Rb, Pb, Zr, and Hf. The rare earth element data for LEW 85305 plagioclase grains varies by about an order of magnitude. The general pattern is a negative slope, with an average La/Yb ratio of 37.8. All grains show a strong relative enrichment in Eu, with an average Eu* value of 28.

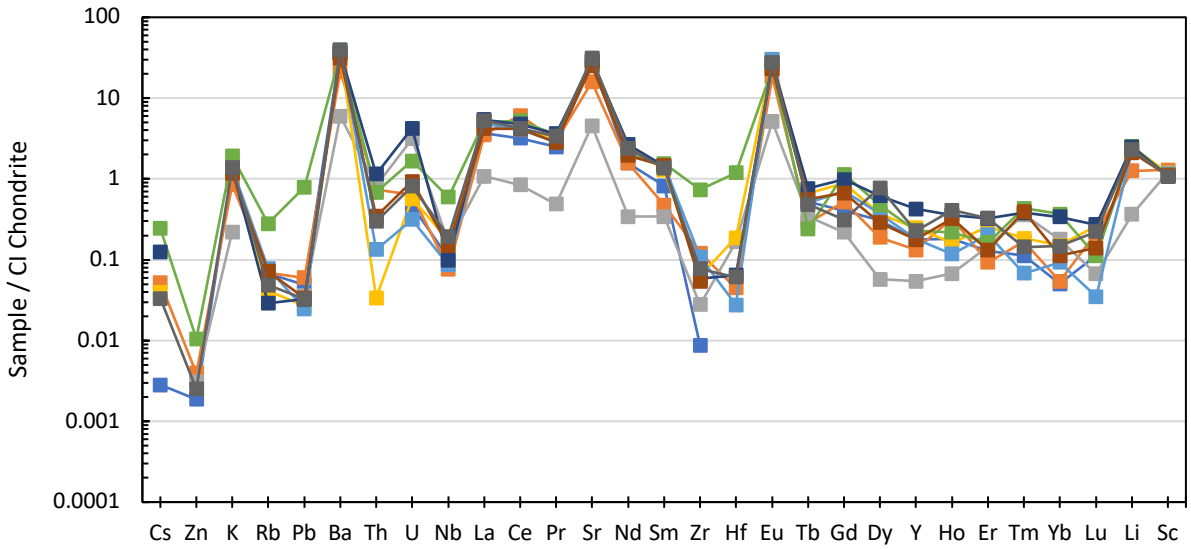

Figure 28. Incompatible trace element diagram for LEW 85305 plagioclase grains. CI chondrite normalization from McDonough and Sun (1995).

The trace element diagram for NWA 1000 varies by about an order of magnitude (Figure 29). The general pattern is a slightly negative slope, where they have higher abundances in the more incompatible elements, and lower abundances of the less incompatible elements. Compared to the general pattern, there are higher abundances of K, Ba, Sr, Eu, Li, and Sc, and lower abundances Cs, Zn, Rb, and Pb. Zirconium varies from in line with the trend to much lower. The rare earth element data for NWA 1000 plagioclase grains varies by about an order of magnitude. The general pattern is a negative slope, with an average La/Yb ratio of 6.1. All grains show a strong relative enrichment in Eu, with an average Eu* value of 104.

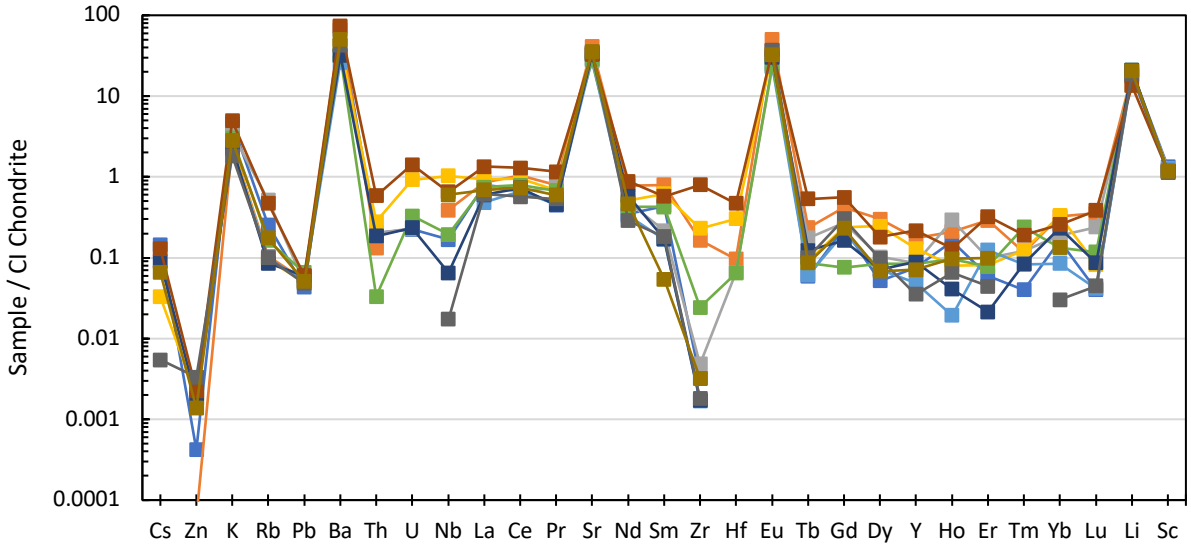

Figure 29. Incompatible trace element diagram for NWA 1000 plagioclase grains. CI chondrite normalization from McDonough and Sun (1995).

The trace element diagram for NWA 1923 varies by about an order of magnitude within the main set of grains, and similar to BTN 00300, has three grains with anomalously high K/Ca ratios, 22 times higher (Figure 30). The general pattern for both sets is a negative slope, where they have higher abundances in the more incompatible elements, and lower abundances of the less incompatible elements. The anomalous grains have higher abundances of almost all elements. Compared to the general trend, both sets have higher abundances of Ba, Eu, Li, and Sc, but the normal grains are also higher in Sr while the anomalous grains are higher in Zr and Hf. Both sets have lower abundances of Cs, Zn, K, and Rb, and the normal grains are also lower in Pb, Zr, and Hf. The rare earth element data for NWA 1923 also shows two sets of plagioclase grains, with little variability within each set. The higher trend has only a slight relative Eu enrichment, while the lower trend shows a strong relative Eu enrichment, with an average Eu* value of 135. The general shape of both trends is a negative slope, with an average La/Yb ratio of 13.2.

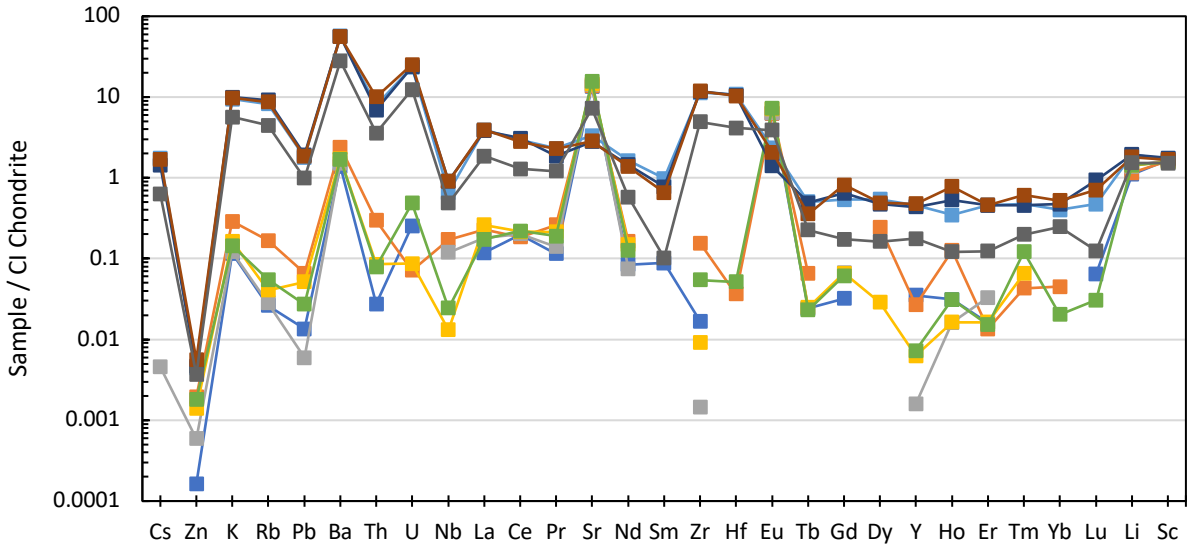

Figure 30. Incompatible trace element diagram for NWA 1923 plagioclase grains. CI chondrite normalization from McDonough and Sun (1995).

The trace element diagram for PCA 92145 varies by less than two orders of magnitude across most elements. (Figure 31). Barium, Sr, and Sc show very little variance. The general pattern is a slightly negative slope, where they have higher abundances in the more incompatible elements, and lower abundances of the less incompatible elements. Compared to the general trend, there are higher abundances of Ba, U, Sr, Eu, Li, and Sc, and lower abundances of Cs, Zn, Rb, and Pb. Zirconium and Hf range from higher to lower than the general trend among the grains measured. The rare earth element data for PCA 92145 plagioclase grains varies by one and a half orders of magnitude on the more incompatible trace element side of the diagram and a little over an order of magnitude on the less incompatible side. The general pattern is a slight negative slope, with an average La/Yb ratio of 8.9. All but three grains show a relative enrichment in Eu, with an average Eu* value of 22 (excluding those 3 grains.) Those grains, like in BTN 00300 and NWA 1923, have anomalously high K/Ca ratios, 8x higher on average.

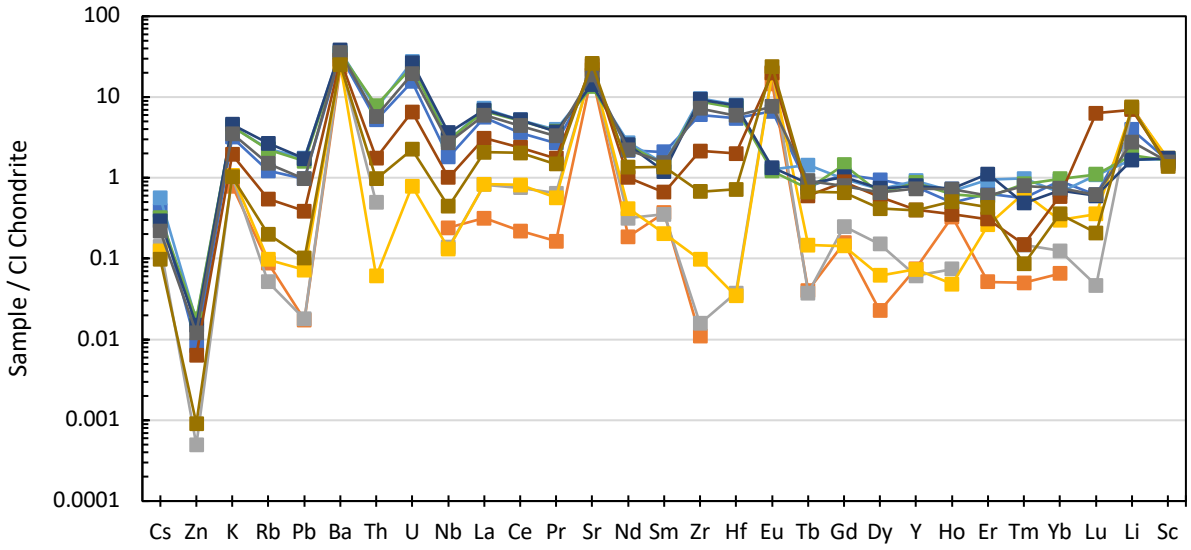

Figure 31. Incompatible trace element diagram for PCA 92145 plagioclase grains. CI chondrite normalization from McDonough and Sun (1995).

The trace element diagram for QUE 97053 varies by about an order of magnitude across all grains except one anomalous grain that has much higher abundances (Figure 32). This grain, as in BTN 00300, NWA 1923, and PCA 91245, has an anomalously high K/Ca ratio, 4x higher than the average normal grain. In the rest of the grains, most elements vary by about an order of magnitude, with Ba, Sr, Hf, Eu, Li, and Sc showing very little variance. The general pattern is shape is a flat pattern. Compared to the general trend, there are higher abundances of Ba, Sr, Eu, Li, and Sc, and lower abundances of Zn, Pb and Zr. The anomalous grain has a slightly negative slope, with higher abundances in the more incompatible elements, and lower abundances of the less incompatible elements. It has a lower relative abundance of Nb, so relative Sr anomaly, and a smaller positive Eu anomaly than the other grains. The rare earth element data for QUE 97053 plagioclase grains varies by about an order of magnitude, with the exception of the anomalous grain. The general pattern is a negative slope, with an average La/Yb ratio of 2.7. All grains show a strong relative enrichment in Eu, with an average Eu* value of 131, excluding the anomalous grain, which has a Eu* value of 2.

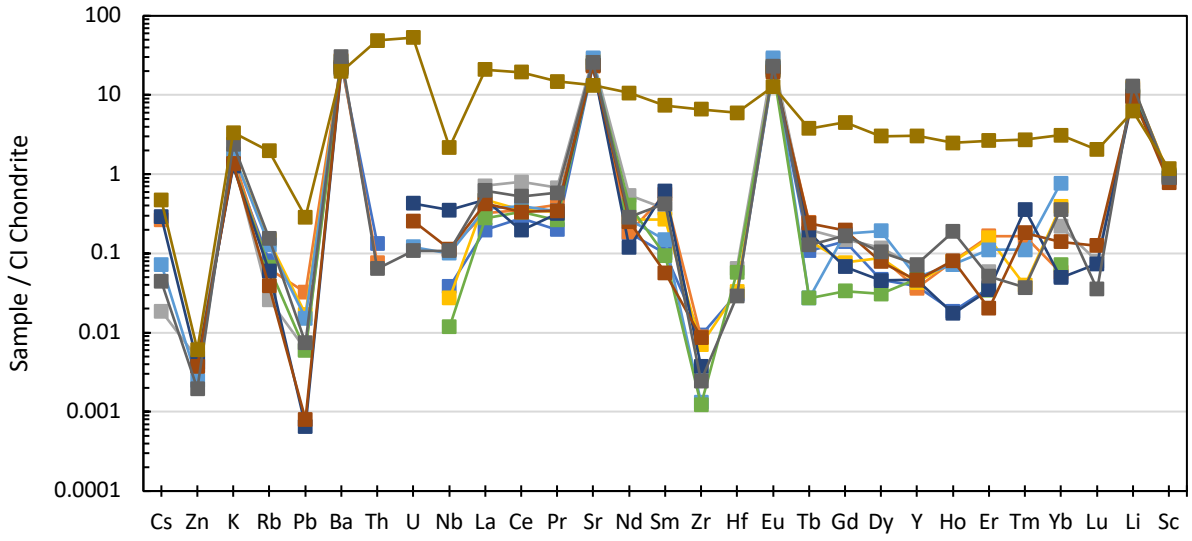

Figure 32. Incompatible trace element diagram for QUE 97053 plagioclase grains. CI chondrite normalization from McDonough and Sun (1995).

In order to directly compare samples, the average of all plagioclase grains for each sample is given in Figure 33. Overall, the eucrites have good agreement in their relative abundances of trace elements but about an order of magnitude variation in their absolute abundances. All samples show the same general pattern of a negative slope, having higher relative abundances in the more incompatible elements, and lower relative abundances in the less incompatible elements. They all show strong depletions in Cs, Rb, and Pb, and enrichments in Ba, Sr, Eu, Li, and Sc. Th, U, Zr, and Hf show more variation than most other elements.

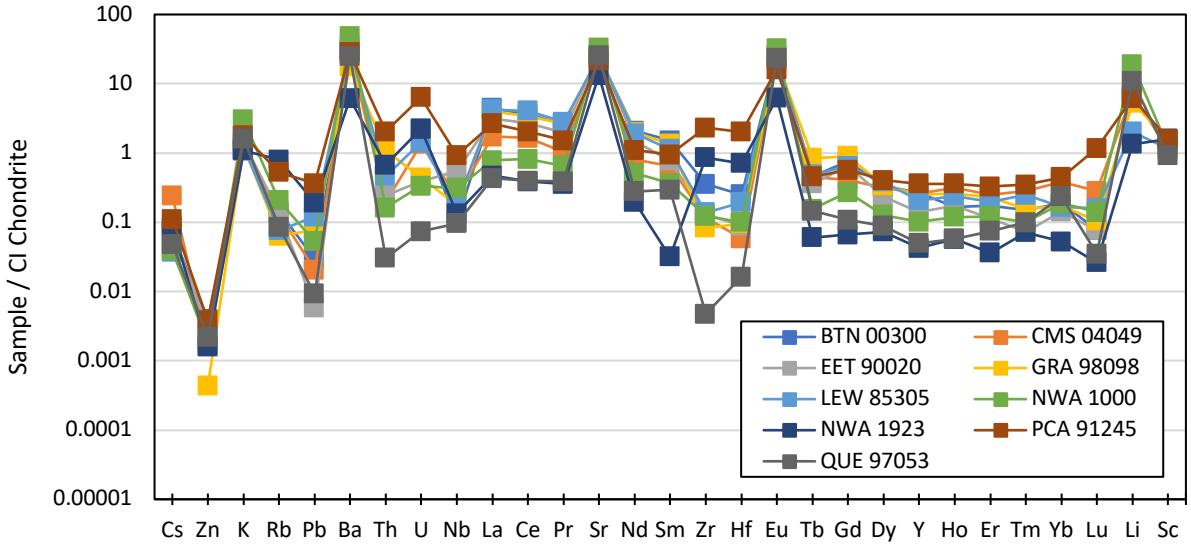

Figure 33. Incompatible trace element diagram of average plagioclase grain composition for each eucrite. To see range of values for each eucrite, see individual diagrams above. CI chondrite normalization from McDonough and Sun (1995).

The REE abundances of average compositions for plagioclase grains measured for each eucrite sample are given in Figure 34. Overall, the eucrites have very similar patterns of trace elements but about an order of magnitude variation in their absolute abundances. NWA 1923 has lower abundances of Sm compared to the general trend. All samples show the same general pattern of a negative slope, with an average La/Yb ratio of 19.6. They all show relative enrichments in Eu, with an average Eu* value of 60.

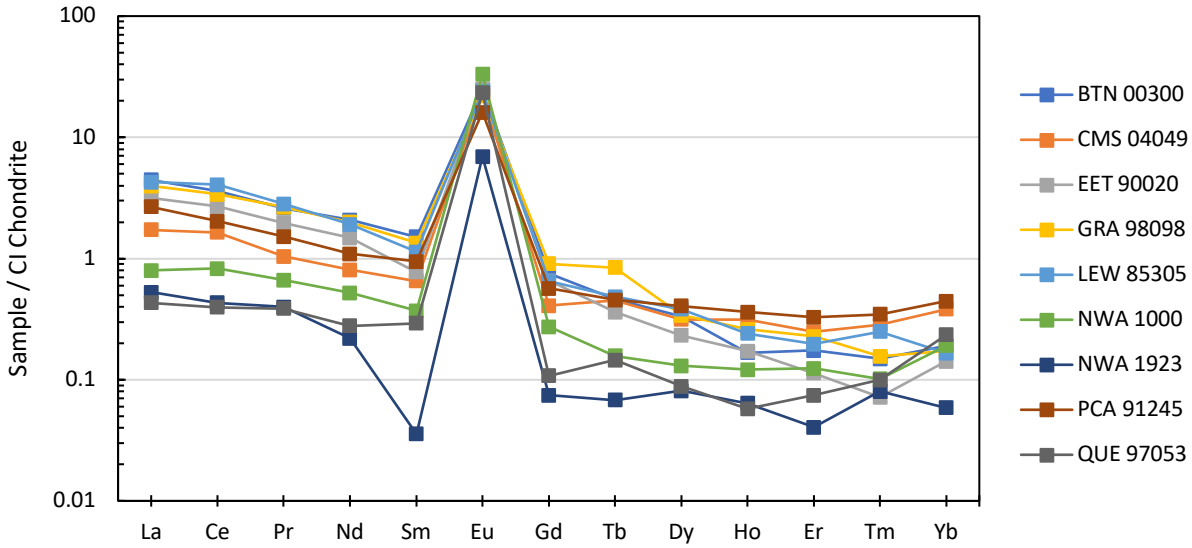

Figure 34. Rare earth element diagram for average plagioclase grain compositions in eucrites. CI chondrite normalization from McDonough and Sun (1995).

3.4.3 Compositions of ALHA 81001 & Fusion Crust

All of the same measurements as those reported for the nine previously described samples were attempted on ALHA 81001. However, while this sample ended up being too fine-grained to distinguish discrete phases, the data is still informative. The major element abundances are: 57 wt. % SiO, 9.9 ± 5.4 wt. % CaO, and 28 ± 4.6 wt. % FeO. The incompatible trace element diagram (Figure 35) varies by a little over an order of magnitude across most

elements. Zirconium and Hf vary by about two orders of magnitude. The general pattern is very flat, with lower abundances of Cs, Zn, K, and Rb.

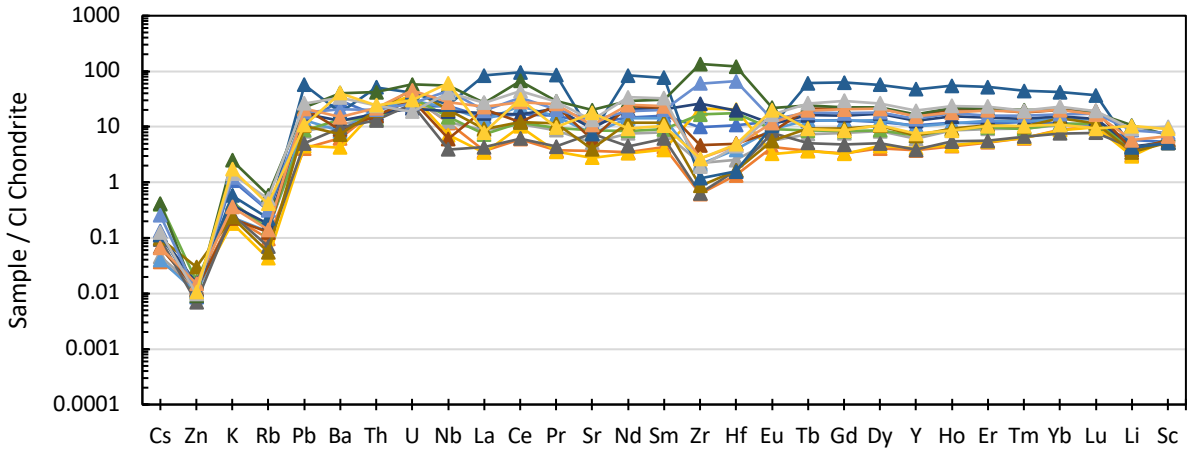

Figure 35. Incompatible trace element diagram for spots measured in the eucrite ALHA 81001. CI chondrite normalization from McDonough and Sun (1995).

The rare earth element diagram (Figure 36) varies by about one and a half orders of magnitude. The pattern is very flat, with an average La/Yb ratio of 1.10. The Eu* values range from 0.15 to 2.10, with an average of 0.75. Many of the grains show an enrichment in Ce.

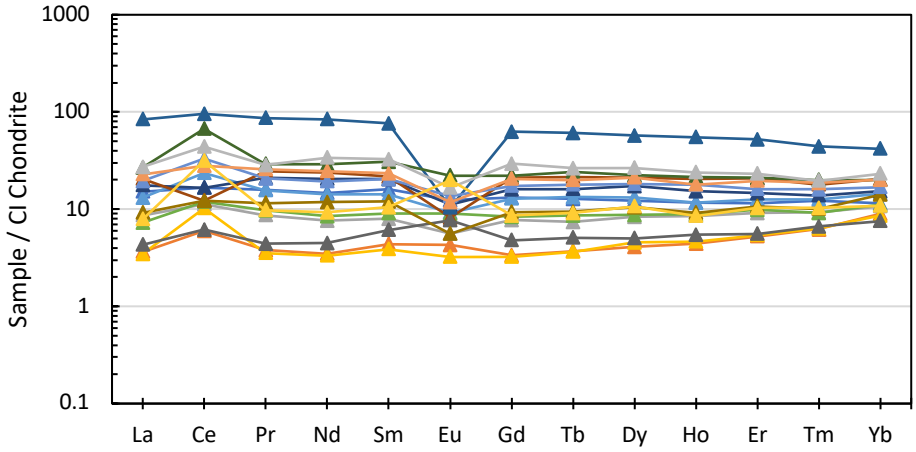

Figure 36. Rare earth element diagram for spots measured in the eucrite ALHA 81001. CI chondrite normalization from McDonough and Sun (1995).

The average measurements of the fusion crust (for the samples that contained it) as well the average of all ALHA 81001 spots is plotted in Figure 37. The general pattern is very flat,

with EET 90020 and ALHA 81001 having a very slight negative slope, higher by less than an order of magnitude on the more incompatible side. Compared to the general trend, they all have lower abundances of Cs, Zn, K, Rb, and Pb, and slight depletions in Li and Sc. EET 90020 and ALHA 81001 show lower abundances of Sr and Eu, and EET 90020 shows a lower abundance of Nb.

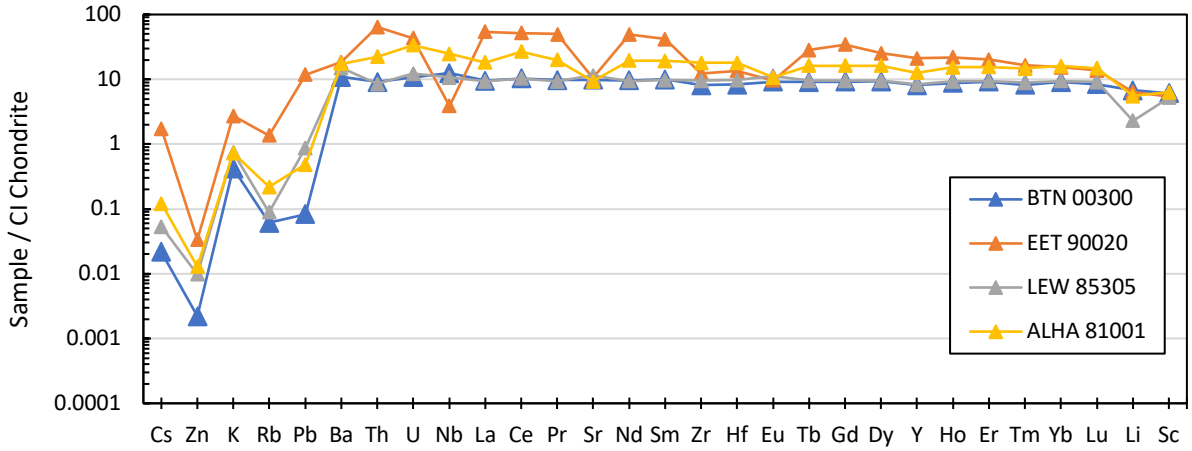

Figure 37. Incompatible trace element diagram for average ALHA 81001 versus average fusion crust compositions measured for BTN 00300, EET 90020, and LEW 85305. CI chondrite normalization from McDonough and Sun (1995).

3.4.4 Modal Reconstructions

Using the plagioclase and pyroxene data from this study and modal percentages, bulk rock reconstructions were calculated assuming that plagioclase and pyroxene make up 100% of the sample. While this is clearly not the case (Mayne et al., 2009; Dhaliwal et al., in review), these phases do make up the large majority of the rock and enable assessment of the relative role of minor phases. All other phases, such as oxides, sulfides, apatites, silica-rich phases, and the mesostasis, are minor phases, accounting to a few percent combined.

Table 5. Plagioclase and pyroxene model percentages from this study, Dhaliwal et al. (in review), and Mayne et al. (2009)

	Plagioclase			Pyroxene		
	This Study	Dhaliwal	Mayne	This Study	Dhaliwal	Mayne
BTN00300	24%	24%	48%	74%	74%	46%
CMS 04049	44%	35%		54%	65%	
EET 90020	22%	14%	50%	72%	85%	49%
GRA 98098	28%	23%	41%	69%	76%	50%
LEW 85305	31%	11%	35%	67%	83%	60%
NWA 1000	23%	24%		76%	76%	
NWA 1923	22%	22%		75%	78%	
PCA 91245	41%	77%		59%	23%	
QUE 97053	35%	40%	51%	65%	60%	48%

A combination of the bulk rock data from Dhaliwal et al., the fusion crust data from this study, and three different modal reconstructions using the three sets of modal percentages (Table 5) are shown in the following figures (Figure 38 to Figure 41). Only BTN 00300, EET 90020, and LEW 85305 had sufficient fusion crust present on the sample to measure. Because the whole sample was too fine grained to measure distinct phases, ALHA 81001 can also be used as a bulk measurement like fusion crust. Mayne et al. (2009) measured many eucrites, but only five overlap with this study: BTN 00300, EET 90020, GRA 98098, LEW 85305, and QUE

97053. In the interest of space, and to avoid repetition, a representative selection of these modal recombination graphs is shown.

The modal reconstructions for BTN 00300 are shown in Figure 38. The bulk and fusion crust measurements are almost identical. All three modal reconstructions underestimate abundances the more incompatible elements but align closely with the bulk and fusion crust measurements on the less incompatible side, as well as with the moderately volatile elements like Cs, Zn, K, Rb, and Pb. The reconstruction using Mayne's modal percentages shows positive Sr and Eu anomalies, likely remnants of the plagioclase signature. All reconstructions show a strong depletion in Nb.

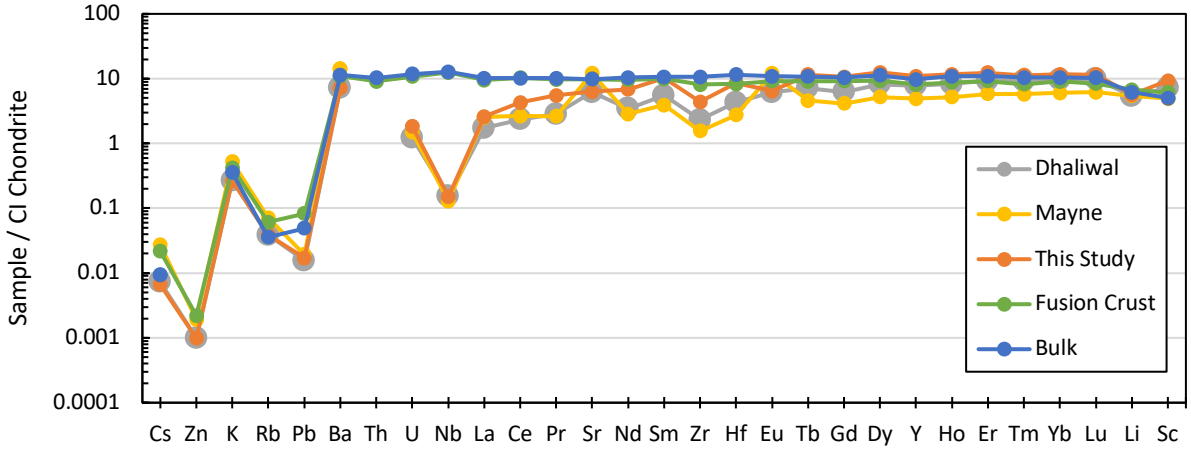

Figure 38. Modal reconstruction of BTN 00300. CI chondrite normalization from McDonough and Sun (1995).

The modal reconstructions for EET 90020 are shown in Figure 39. The fusion crust measurements have slightly higher abundances than the bulk measurements for most elements. Both fusion crust and bulk measurements show negative relative Nb, Sr, and Eu anomalies, and well as a negative slope, having higher relative abundances in the more incompatible elements, and lower relative abundances in the less incompatible elements. All three modal reconstructions have a positive slope, having lower relative abundances in the more

incompatible elements, and higher relative abundances in the less incompatible elements. These reconstructions underestimate abundances of most elements but align more closely with the bulk and fusion crust measurements on the less incompatible side, and with moderately volatile elements such as Cs, K, and Rb. All modal reconstructions have a positive relative Sr anomaly, and the reconstruction using Mayne's modal percentages has a positive relative Eu anomaly.

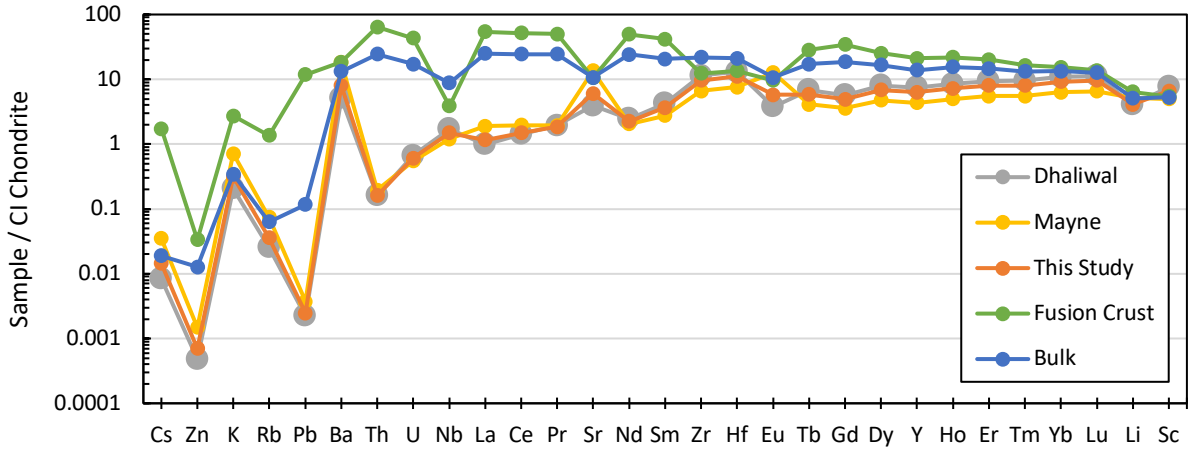

Figure 39. Modal reconstruction of EET 90020. CI chondrite normalization from McDonough and Sun (1995).

The modal reconstructions for LEW 85305 are shown in Figure 40. The bulk and fusion crust measurements are almost identical, except for Pb. All three modal reconstructions underestimate abundances of the more incompatible elements but align closely with the bulk and fusion crust measurements on the less incompatible side, as well as with the moderately volatile elements like K, Rb, and Pb. The reconstruction using Dhaliwal et al.'s modal percentages shows negative relative Sr and Eu anomalies. All reconstructions have low abundances of Cs and Zn. The bulk and fusion crust measurements for Cs and Zn are also low, but not quite as much as the reconstructions.

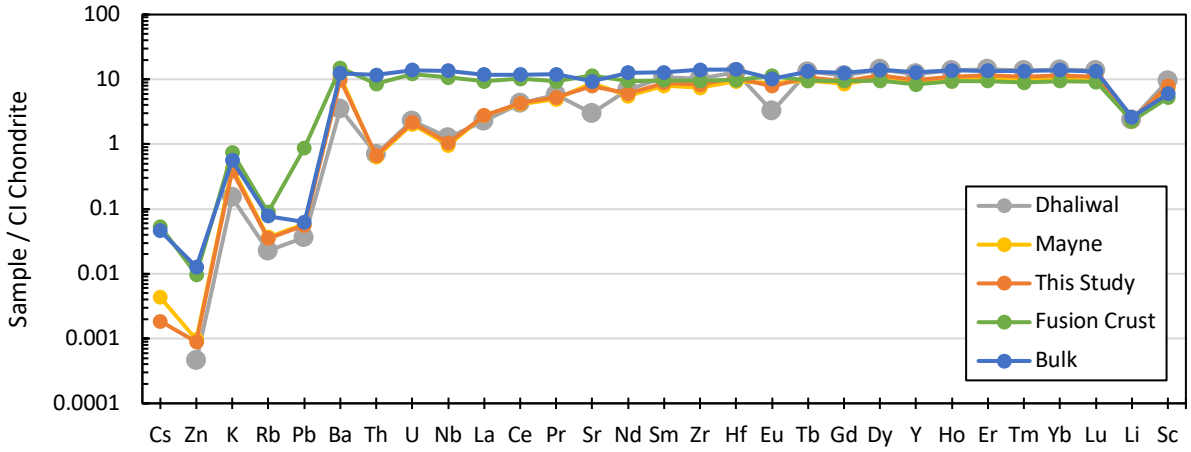

Figure 40. Modal reconstructions for LEW 85305. CI chondrite normalization from McDonough and Sun (1995).

The modal reconstructions for QUE 97053 are shown in Figure 41. There was no fusion crust present on this sample to measure. All three modal reconstructions underestimate abundances of most elements but align more closely with the bulk measurements on the less incompatible side, as well as with the MVE's like Cs, Zn, K, Rb, and Pb. All three reconstructions show positive relative Sr and Eu anomalies, as well as a positive relative U anomaly.

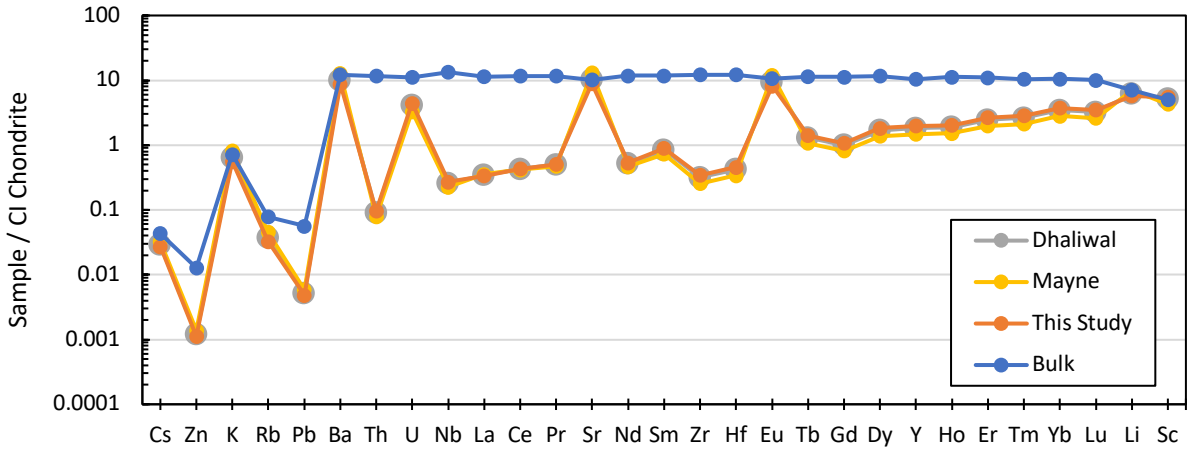

Figure 41. Modal Reconstruction of QUE 97053. CI chondrite normalization from McDonough and Sun (1995).

The modal reconstructions for NWA 1923 are shown in Figure 42. The modal reconstructions align closely with the bulk measurements across the board, but slightly underestimate the bulk measurements for some of the more incompatible elements like U, Nb, La, Ce, Pr, Nd, and Sm. NWA 1923 had anomalously low abundances of most elements in both plagioclase and pyroxene measurements in this study, as well as in the bulk measurements. Dhaliwal et al. (in review) suggest that NWA 1923 is more accurately described as a cumulate eucrite.

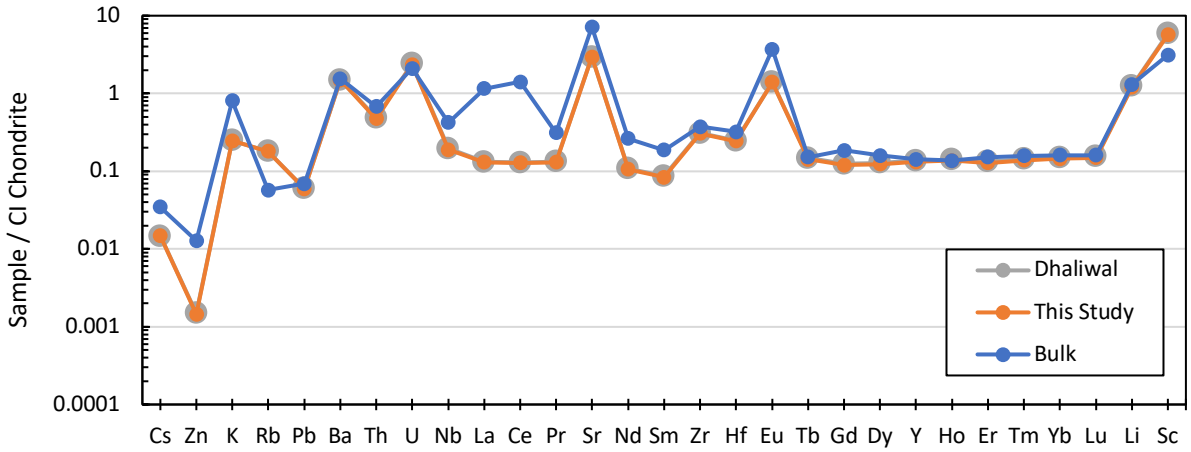

Figure 42. Modal reconstructions for NWA 1923. CI chondrite normalization from McDonough and Sun (1995).

4. Discussion

4.1. Assessment of primary crystallization products versus impact melts

As outlined in section 3.1, the textures among the ten samples of this study vary substantially, from fine-grained acicular textures, to medium-grained granular textures, to coarse grained subophitic textures. These textures and can potentially be used to discern information about the history of the samples.

Allan Hills 81001 and NWA 1000 both have skeletal, acicular structures, with elongate, overlapping grains with no organized structure or orientation. This texture is formed from the rapid cooling, or quenching, of a melt. On a body like Vesta, the most likely explanation of this would be melting and rapid cooling as the result of a high-energy impact. The young $^{40}Ar/^{39}Ar$ age of only 3.693 Ga (Fu et al., 2012) confirms that the crystallization of ALHA 81001 occurred some ~850 million years after the asteroid, from an impact. While NWA 1000 is much coarser-grained, the similarity of its texture to ALHA 81001 means that it is also likely the result of an impact melt.

The next group of samples with similar textures includes BTN 00300, EET 920020, LEW 85305, GRA 98098, and NWA 1923. These samples have a more granular or granoblastic texture than a typical basalt: more equidimensional grains, fairly uniform grain size, well-defined grain boundaries, and abundant triple-junctions. This is a typical texture in rocks that have experienced some level of thermal metamorphism, and reorganization of the preexisting texture to become more uniform. In some of the samples, the remnants of a subophitic texture are visible, further supporting the argument that these samples represent rocks that have been thermally metamorphosed from their original igneous state, with the ultimate heat source for this metamorphism being from late-stage impacts.

The final group of samples contains CMS 04049, PCA 91245, and QUE 97053. These samples have a coarser grained, subophitic texture, with elongate plagioclase randomly oriented and touching, with pyroxene in between. This is a classic igneous crystalline texture, indicating that these samples have experienced very little textural modification since they were crystallized from a basaltic melt.

In order to compare the compositions of the three groups, incompatible trace element diagrams using average values for granular and subophitic texures are shown (Figure 43 and Figure 44). Only NWA 1000 is shown to represent the impact melts because individual mineral data were not collected for ALHA 81001. Northwest Africa 1923 was omitted from the average of granular samples because of its anomalously low composition, likely due to its origin as a cumulate eucrite (Dhaliwal et al., in review). There are differences between the granular and subophitic trends, particularly for Zr and Hf and increasing light REE abundances in plagioclases and REE abundances in pyroxene in the granular samples. Due to the limited sample size of four granular samples and three subophitic samples, it is unclear if these apparent geochemical differences actually represent significant differences in composition between the granular and subphitic samples. Sarafian et al. (2013) also found no apparent correlation between apatite composition and degree of metamorphism.

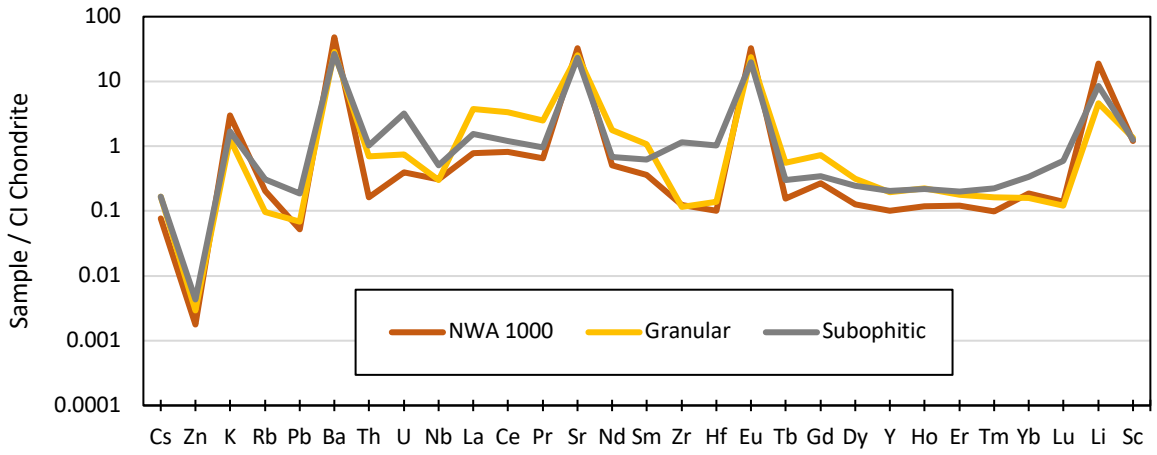

Figure 43. Incompatible trace element diagram for plagioclase grains in average granular eucrites, average subophitic eucrites, and NWA 1000. CI chondrite normalization from McDonough and Sun (1995).

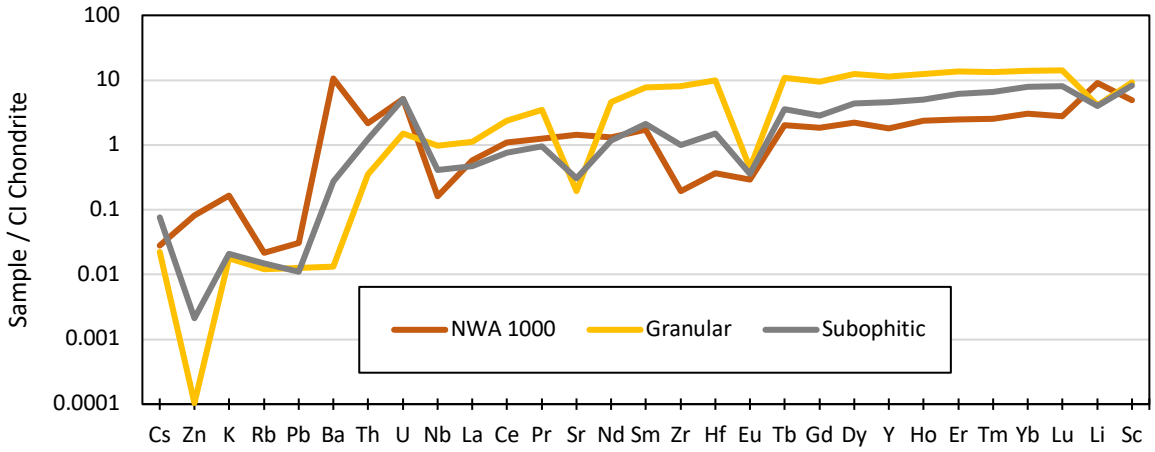

Figure 44. Incompatible trace element diagram for pyroxene grains in average granular eucrites, average subophitic eucrites, and NWA 1000. CI chondrite normalization from McDonough and Sun (1995).

4.2. Eucrite REE and incompatible trace element compositions for plagioclase and pyroxene

In general, most samples displayed similar relative rare earth element (REE) and incompatible trace element patterns, with absolute abundances varying by about an order of magnitude across the range of samples. These data are shown collectively in Figure 45. For the plagioclase grains, this pattern is a slight negative slope, where they have higher abundances in the more incompatible elements, and lower abundances of the less incompatible elements. All plagioclase grains showed positive relative Eu and Sr anomalies, as well as higher abundances of Ba, Li, and Sc. They all have lower abundances of the moderately volatile elements Cs, Zn, Rb, and Pb. In terms of their REE abundances, they are similar to previously published data (Hsu and Crozaz, 1996). For pyroxene grains, the general pattern is a slight positive slope, where they have lower abundances in the more incompatible elements, and higher abundances

of the less incompatible elements. All pyroxene grains show negative relative Eu and Sr anomalies, and lower abundances of the moderately volatile elements Cs, Zn, K, Rb, and Pb.

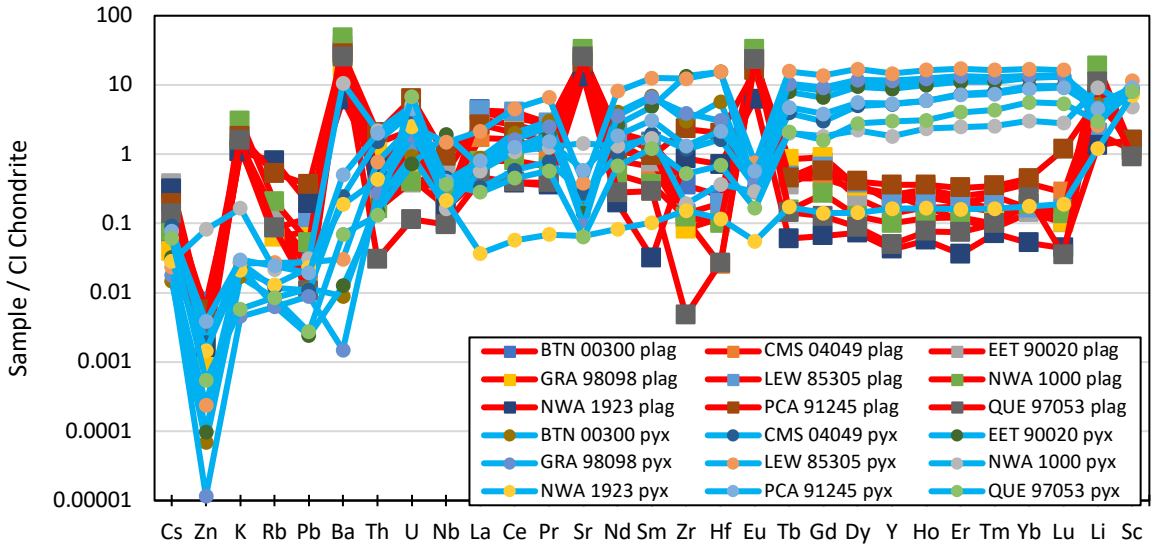

Figure 45. Incompatible trace element diagram showing average plagioclase and pyroxene grain compositions for each eucrite. CI chondrite normalization from McDonough and Sun (1995).

Other clear differences between the plagioclase and pyroxene trends, as seen in Figure 45, are the relative Eu and Sr anomalies: positive anomalies in the plagioclase, and negative in the pyroxene. This is expected and helps to confirm that igneous processes very similar to those that form terrestrial and lunar basalts were at work on Vesta. As the magma cooled, plagioclase grains crystallized first, preferentially incorporating the Eu^{2+} and Sr^{2+} ions, substituting for Ca^{2+} ions. This caused the plagioclase grains to become enriched, and the magma to become depleted in Eu. From this Eu and Sr depleted magma, the pyroxene grains crystallized, incorporating the depleted Eu and Sr signature from the magma. Additionally, this graph shows that K, Rb, and Pb are more abundant in the plagioclase grains. The other MVE's measured, Cs and Zn, exist in similar abundances in both minerals.

While the fine grained texture of ALHA 81001 did not allow the measurement of discrete phases, when compared to the bulk measurements and fusion crust measurements, as in Figure 37, its composition can be described as falling within the normal trend. One unusual aspect of the ALHA 81001 data is the positive Ce anomalies in about half of the spots measured suggesting possible oxidation as Ce^{4+}.

Northwest Africa 1923 has a strikingly different composition from the rest of the samples, best seen in its pyroxene incompatible trace element diagram, Figure 22. It has lower abundances by more than an order of magnitude in most trace elements compared to the average of all other pyroxene grains. In the plagioclase grains, the difference is not as dramatic, but it is on the low end of the range. This overall depletion is confirmed by the bulk data and modal reconstruction in Figure 42. Dhaliwal et al. (in review) suggests that NWA 1923 is more accurately described as a cumulate eucrite. Northwest Africa 1000 had unique features in its pyroxene data as well: flatter overall pattern, no Sr anomaly, slight positive Li anomaly, and higher abundances of Zn, K, and Ba.

Four samples had anomalous plagioclase grains: BTN 0030, NWA 1923, PCA 91245, and QUE 97053. These anomalous grains were anomalously high in K, with K/Ca ratios 4 to 22 times greater than the rest of the plagioclase grains in the sample. Additionally, they do not show a significant Eu anomaly. Although these grains visually appeared to be plagioclase when selecting the spots to measure, this anomalous data suggests that they are instead a more evolved feldspar, similar to those discovered previously in eucrites (e.g., McQuaig et al., 2019). Two of these samples fall into the granular textural category, and two of these samples fall into the subophitic category, so these anomalous grains do not appear to correlate with texture.

4.3. Analysis of modal reconstructions and comparison with bulk rock and fusion crust compositions

From the modal reconstruction data, Figure 38 through Figure 42, it is clear that the fusion crust measurements in this study are a good analog for bulk rock measurements. They are almost identical, except for EET 90020, in which the fusion crust is a little more enriched, has a more positive slope, and more negative Sr and Eu anomalies. Since this is the signature of the pyroxene grains measured in this study, it is likely that the fusion crust measured in EET 90020 contained a greater portion of pyroxene than the bulk rock, or the ablation pit for the fusion crust spots also measured adjacent pyroxene grains. Examining the photomicrograph maps, a few of the spots measured were directly adjacent to pyroxene grains, further evidence for this hypothesis. Fusion crust analyses have previously been done on meteorites (e.g., Day et al., 2006), and while perhaps not a perfect match for the bulk rock (Thaisen & Taylor, 2009) are a good first approximation, especially for low mass meteorites.

In Table 5, it is apparent that the modal percentages reported by Mayne et al. (2009) were either calculated significantly differently than in this study, or that the sections that they studied have quite different distributions of plagioclases and pyroxene. The percentages from this study and Dhaliwal et al. (in review) were calculated using the same software and method, and are very similar despite three different users making the estimates (BK, JMDD, J. Dhaliwal). Minor differences between these estimates can be attributed to cropping the photomicrograph images to different areas of the sample. A visual estimation of the photomicrograph maps confirms that, in the sections measured in this study, the pyroxene to plagioclase ratio is closer to 4:1 or 3:1, rather than 1:1, like Mayne et al. (2009) percentages

indicate. The fact that all of the reconstructions using Mayne et al.'s percentages have positive Eu and Sr anomalies, while many of the reconstructions using the percentages from this study do not, and more closely mimic the bulk rock, also indicates that Mayne et al.'s percentages overestimate the plagioclase content of the sample. This could be due to heterogeneities within or between samples of the same eucrite, or due to calculation of percentages based on the electron microprobe maps in the Mayne et al. (2009) study.

Regardless of the differences between the modal percentages, the reconstructions show limited differences between any of the modal reconstructions. The only significant differences are in the Sr and Eu anomalies, and in some of the heavily depleted elements like Cs and Zn, where the abundances are very low. All reconstructions underestimate the bulk measurements in the more incompatible elements, but most accurately reconstruct the elements on the less compatible side. This indicates that the elements missing from these reconstructions exist in the minor accessory phases. Missing Nb would likely be in the oxide phases (e.g., ilmenite), while Zr and Hf would likely be in zircon or baddeleyite, and the missing more incompatible REE's would likely be in phosphates like apatite. It follows that the most incompatible elements would be more abundant in the final accessory phases to crystallize, and not the major silicate mineral phases. However, in the moderately volatile elements important to this study, all reconstructions successfully recreate the lower abundances of Cs, Zn, K, Rb, and Pb, suggesting the abundances of these elements are not significant in late-stage phases, so that correlations with the isotopes of these elements and apatite compositions may merely be coincidental (e.g., Sarafian et al., 2017; 2019).

4.4. Abundances of the MVE (Cs, Zn, K, Rb, and Pb) in eucrites

Although highly volatile elements were not targeted in this study, due to the expected levels of such volatiles in the major phases, and scarcity of accessory minerals large enough to measure with the LA-ICP-MS set-up that we used (i.e., 100 micrometer spot sizes), moderately volatile elements such as Cs, Zn, K, Rb, and Pb can be used as a proxy for these more volatile elements. A method first employed by Albarède et al. (2014) is to use a ratio between a refractory element and a moderately volatile element that have similar characteristics and behaviors. These ratios are constant in terrestrial mid-ocean ridge basalts and ocean island basalts, indicating that the two elements are not fractionated during melting or crystallization on Earth; by extension, this relation is inferred for Vesta and the Moon, too. Therefore, if the ratio is lower, it shows that the samples are depleted in that element. The ratios examined in this study are Rb/Ba, Rb/Sr, and Zn/Fe. One important difference between this study and Albarède et al. (2014) is that their study measured the ratios in lunar volcanic glass. Due to the lack of Vestan volcanic glass samples, this study examined individual minerals, both plagioclase and pyroxene. It is important to note that not all ratios work well for both plagioclase and pyroxene due to their drastically different chemistry. Because plagioclase has higher abundances of Rb, Ba, and Sr, and is very low in Fe, it is more useful to look at Rb/Ba and Rb/Sr. Conversely, Zn/Fe works much better when looking at pyroxenes due to its higher levels of Zn and Fe, and low Rb, Ba, and Sr.

Rubidium/Ba diagrams from both this study and Albarède et al. (2014) are shown in Figure 46. Both show a contoured heat map of mid-ocean ridge basalt (MORB) and ocean island basalt (OIB) data (Albarède et al., 2014) representing the terrestrial equivalent of the lunar

volcanic glass and eucrites. This MORB and OIB data shows a consistent Rb/Ba value of about 0.1 across a few orders of magnitude range in Ba values, indicating that these elements are not fractionated during melting or crystallization. The left graph is taken directly from Albarède et al. (2014) and shows that the Rb/Ba ratios of the lunar glasses are indeed depleted by about an order of magnitude. The right graph in the figure shows Rb/Ba data from the eucrite plagioclase grains measured in this study. With the exception of the anomalous sample NWA 1923 and a couple of outlier points, it also shows Rb/Ba ratios depleted by about one to two orders of magnitude from the terrestrial data. The bulk eucrite data shows the same depletion as the plagioclase data, confirming both that this depletion is present, and also that it is valid to use plagioclase instead of volcanic glass. Collectively, these graphs suggest that eucrites may have a similar level of volatile depletion to the Moon for Rb, consistent with MVE loss from Vesta inferred from Rb isotopes (Pringle & Moynier, 2017).

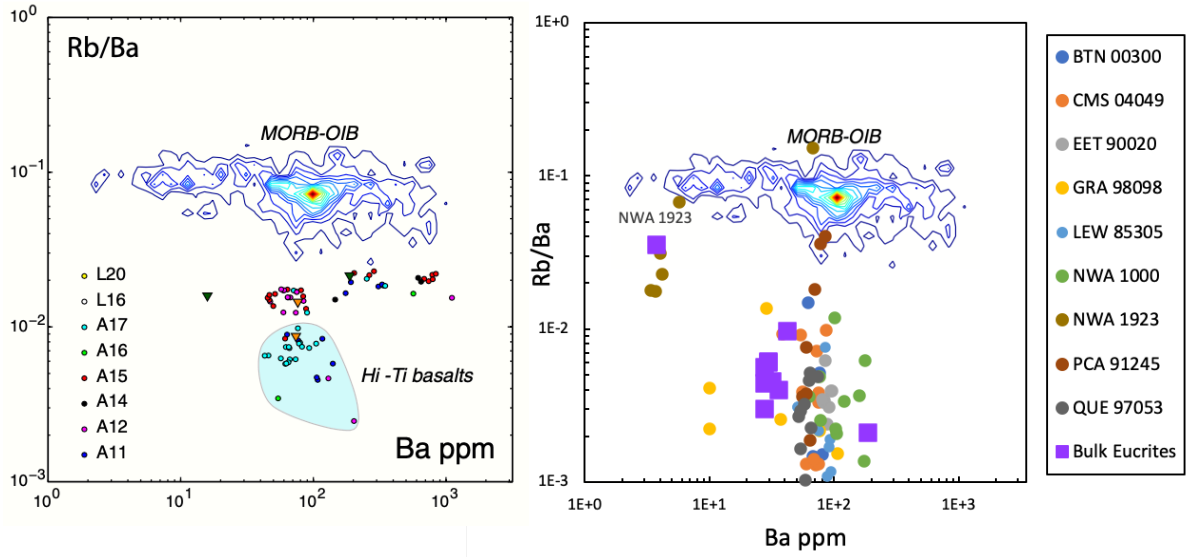

Figure 46. Left: Rb/Ba diagram of lunar volcanic glass from Albarède et al. (2014). Right: Rb/Ba diagram of plagioclase grains measured in this study. MORB-OIB data from Albarède et al. (2014) figure on left. Bulk eucrite data from Dhaliwal et al. (in review.)

Rubidium/Sr data from this study, as well as bulk Eucrite data, is shown in Figure 47. It includes depleted MORB mantle (DMM) and primitive mantle (PM) as terrestrial equivalents to compare the eucrite data to. A caveat with this data, as opposed to the Rb/Ba and Zn/Fe data, is that the terrestrial Rb/Sr values do show significant variability between DMM and PM, suggesting that there were some fractionation effects in melting or crystallization. The eucrite pyroxene data is predictably low in Sr, and the plagioclase data is much more enriched than DMM and PM. The bulk eucrite data falls in between the plagioclase and pyroxene points, illustrating mixing between the two main phases. The bulk data is more enriched in Sr, and has a lower Rb/Sr ratio than both PMM and DM. This might imply that eucrites are depleted, or may simply be due to their enrichment in Sr. These results confirm bulk rock and mineral isochron data for eucrites indicating strong Rb depletion from the eucrite parent body subsequent to its assembly (Moynier et al., 2012; Hans et al., 2013).

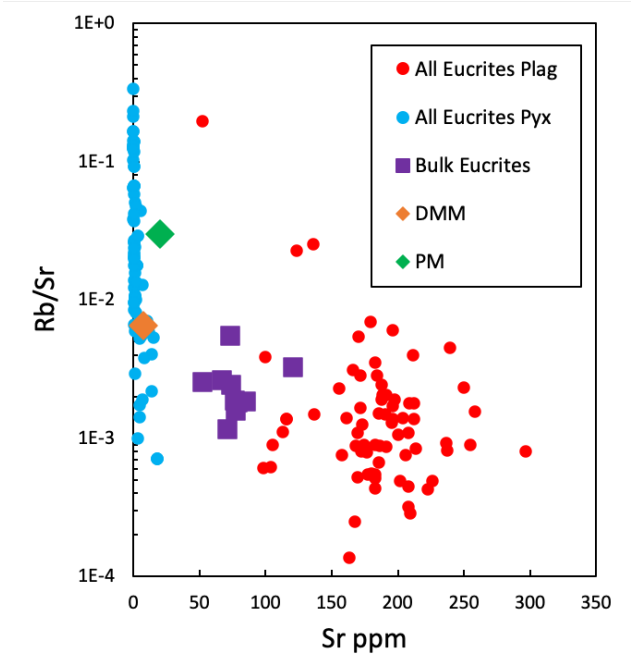

Figure 47. Rubidium/Sr diagram of plagioclase and pyroxene measured in this study. Bulk eucrite data from Dhaliwal et al. (in review), depleted MORB mantle (DMM) data from Workman and Hart (2004), and primitive mantle (PM) data from McDonough and Sun (1995)

Zinc/Fe diagrams using data from this study, as well as Albarède et al. (2014) and Dhaliwal et al. (in review) are shown in Figure 48. The graph on the left shows the Zn/Fe ratios for all pyroxene measurements in this study. The graph on the right shows a contoured heat map of MORB and OIB data (Albarède et al., 2014) representing the terrestrial equivalent of the lunar volcanic glass and eucrites. This MORB & OIB data shows a consistent Zn/Fe value of about 10^{-3} and about 10 wt.% Fe, indicating that these elements are not fractionated during melting or crystallization. It also shows the Zn/Fe values of the lunar volcanic glass measurements from Albarède et al. (2014), which cluster at about 10^{-5}. Also plotted are the Zn/Fe ratios of all plagioclase and pyroxene measurements from this study. The plagioclase grains are predictably low in Fe content, and thus span a very large range of Zn/Fe values, with an average of about 10^{-4}. The pyroxene grains form a neat grouping with a Zn/Fe ratio of about 10^{-5}, overlapping strongly with the lunar volcanic glass grouping. Finally, bulk eucrite Zn/Fe ratios are shown (Dhaliwal et al., in review). These bulk eucrite Zn/Fe values show a mixing trend between the pyroxene and plagioclase endmembers, and are on the higher side of the lunar and pyroxene groupings. Like the pyroxene and lunar volcanic glass data, they also appear to be strongly depleted in Zn compared to MORB and OIB. The very low Zn contents, especially in pyroxene, and apparent mixtures of plagioclase and pyroxene dominating the bulk rock compositions (Figure 48) suggest generally low Zn contents in unbrecciated primary eucrites, possibly indicating that the spread in δ^{66}Zn values measured for eucrites previously (Paniello et al., 2012) reflect mixtures of rocks that have experienced MVE loss as well as impact processes that reenriched Zn.

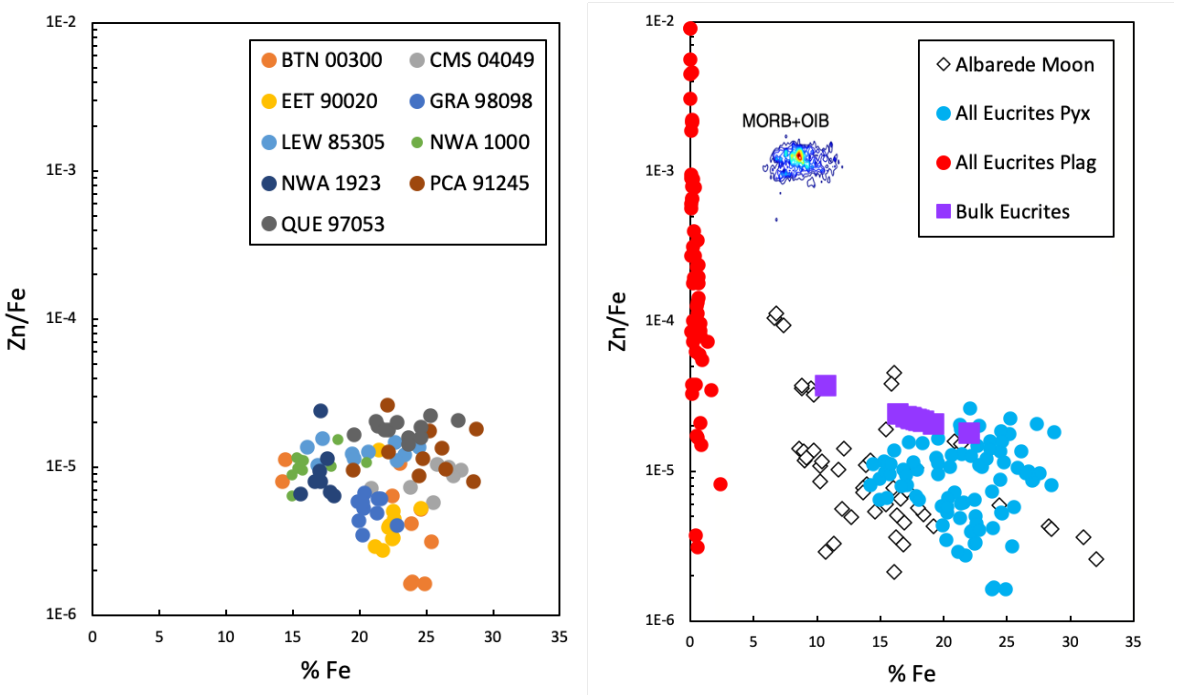

Figure 48. Left: Zinc/Fe diagram of pyroxenes from eucrite samples in this study. Right: Zn/Fe diagram showing MORB & OIB data and lunar volcanic glass values from Albarède et al. (2014). Also Zn/Fe values for all plagioclase and pyroxene samples in this study, and bulk eucrite data from Dhaliwal et al. (in review)

Another way of assessing volatile abundances, also shown in Albarède et al. (2014), is to look at the volatility trend visible when plotting normalized elemental abundances versus a measure of the element's volatility. As a measure of the elements' volatility, Albarède et al. (2014) discussed both 50% condensation temperature (50% T_C) calculated for a gas of solar composition at 10^{-4} bar (Lodders, 2003) and the bond energy between the element and a particular ligand. A 50% condensation temperature is defined as the temperature at which 50% of the element will have condensed out of the solar nebula; volatile elements condense out at lower temperatures than refractory elements. Bond energy refers to the strength of the bond between itself, O, S, Cl, or the element's sublimation energy. In choosing the appropriate ligands, Albarède et al. (2014) showed that these two measured are basically interchangeable (R^2 = 0.96), as seen by the similarity between Figure 49 and Figure 50. In both graphs, the

refractory elements have consistent normalized abundances of ~1 at high 50% T_C and bond energies, and the volatile elements fall along a downward trend, with the slope of this trend indicating the level of volatiles present.

From these graphs it is clear that the Moon, which has the steepest trend, is much more depleted in volatiles than Earth. The eucrite data is not quite as clear. The plagioclase trend is the least steep, flatter even than Earth's. However it is clear that lower normalized abundances in many of the REE and refractory elements (as seen in Figure 33) is altering this trendline, as well as increased normalized abundances in many large-ion lithophile elements. The pyroxene trend, on the other hand, is almost as steep as that of the Moon. The bulk eucrite trend lies between the plagioclase and pyroxene trends, which is expected due to mixing of the two major phases, and thus, is likely the best indicator for this method. This bulk eucrite trend falls somewhere between Earth and the Moon.

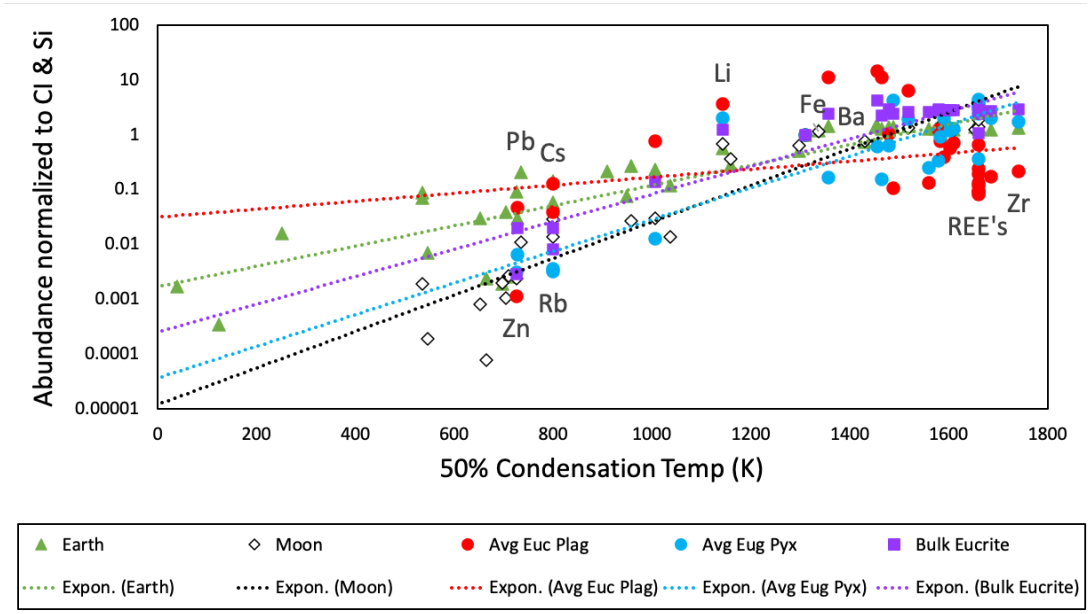

Figure 49. Volatility trend graph of 50% condensation temperature versus elemental abundance normalized to CI chondrite and Si. Earth data from McDonough and Sun (1995), Moon data from Albarède et al. (2014), and Bulk Eucrite data from Dhaliwal et al. (in review).

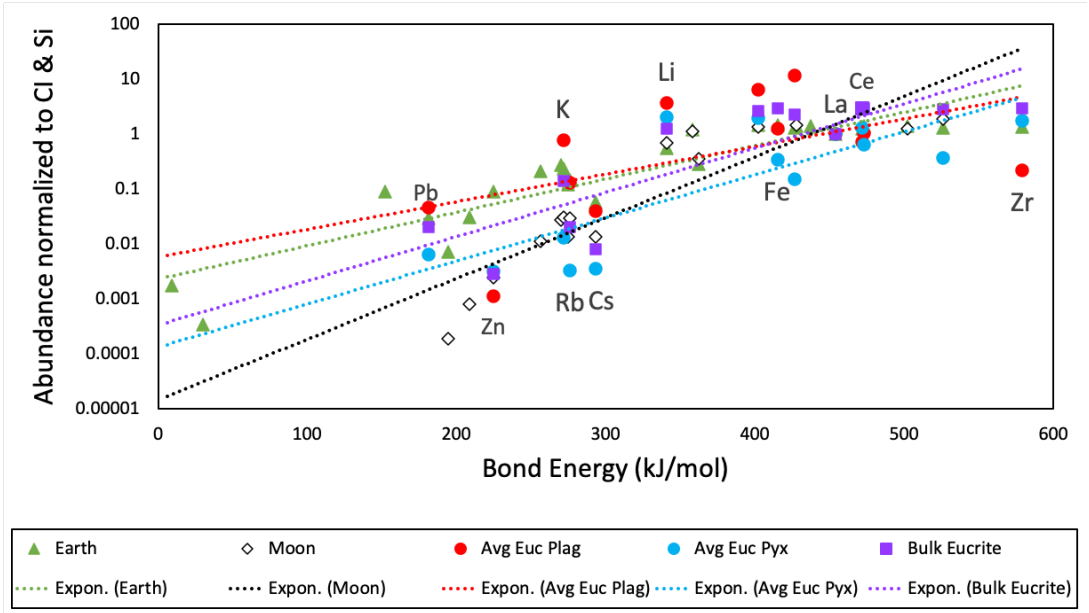

Figure 50. Volatility trend graph of bond energy versus elemental abundance normalized to CI chondrite and Si. Earth data from McDonough and Sun (1995), Moon data from Albarède et al. (2014), and Bulk Eucrite data from Dhaliwal et al. (in review).

The data published by Albarède et al. (2014) was somewhat incomplete, missing the bond energies for many of the elements measured in this study, as well as the elemental abundances of the lunar glass for many different elements measured in this study. By presenting both graphs, these shortcomings are minimized, but a more complete data set would certainly give more accurate results. However, the volatile/refractory element ratios as well as the 50% T_C and bond energy volatility graphs show that eucrites are depleted in volatile elements compared to Earth. Compared to the Moon, it is harder to constrain. The Rb/Ba ratios show similar depletion levels to the Moon, the Zn/Fe ratios show eucrites slightly less depleted than the Moon, and the 50% T_C and bond energy volatility graphs also show that eucrites are not as depleted as the Moon. Likely, eucrites are more depleted than Earth, but not as depleted as the Moon.

These findings are comparable to other published research. Sarafian et al. (2013), analyzing the volatile contents of apatites in eucrites using electron microprobe, found that they were depleted compared to chondritic abundances. Comparing some eucritic apatites to lunar apatites, these authors argued that they have similar volatile compositions, indicating that "the two bodies could have had a similar volatile content, or each of the basalts degassed to varying degrees, ending with apatites with a similar volatile content." Other eucritic apatites examined by those authors were found to be relatively OH-rich, likely from a "relatively undegassed magma", pointing to the "presence of H_2O in the vestian interior." Results from the study support a volatile depleted Vesta, but indicate that volatile loss was probably equal or less to that experienced by the Moon. Sarafian et al. (2014) reports water concentrations in eucritic apatites ranging widely from 668 to 2624 μg/g. Additionally they looked at isotopic ratios of H, C, and N, which they found to be similar between Earth and the eucrites. They argued that the source of volatiles was carbonaceous chondrites, delivered very early in Solar System history. Given the ancient ages of eucrites at about 4.56 Ga, which imply crystallization ages of up to only ~20 Ma after calcium-aluminum-rich inclusion (CAI) formation (the oldest solid materials in the solar system) this volatile depleted signature must have existed from very early on. Thus, it is unlikely that secondary late accretion of chondritic materials has affected the abundances seen in these eucrites. If this late accretion occurred, it may be seen in howardites, or brecciated eucrites, contaminated by such impactors.

Since Vesta is thought to be a differentiated asteroid, it must have undergone a significant level of heat and full or partial melting, forming the very early crust that eucrites are thought to partially represent, and segregating the siderophile elements into the core. However, it is not clear that Vesta underwent a magma ocean phase (e.g., Stolper, 1977; Righter & Drake,

1997; Mandler & Elkins-Tanton, 2013; Dhaliwal et al., in review). On the other hand, according to current paradigms, the Moon was formed from the giant impact of a large body, Theia, into the proto-Earth, resulting in extreme temperatures, a magma ocean, and the vaporization and subsequent loss of volatile elements to space (e.g., Dhaliwal et al., 2018). This impact was likely much more violent and energetic than the processes that formed Vesta, leading to the possibility that the Moon is in fact more depleted than Vesta, contrary to previous assertions (e.g., Halliday, 2001; Day & Moynier, 2014).

5. Conclusions

In this study, twenty-one eucrite thin sections were studied using polarized light microscopy and photomicrograph mapping. Combining the visual cues from microscopy with bulk rock HSE data of the samples to check for contamination, ten samples were selected as pristine and were studied further using LA-ICP-MS. The ten samples selected were ALHA 81001, BTN 00300, CMS 04049, EET 90020, GRA 98098, LEW 85305, NWA 1000, NWA 1923, PCA 91245, and QUE 97053. These samples were measured for abundance of 32 different elements total, consisting of both major and trace elements. Because pyroxene and plagioclase make up the majority of all the samples, approximately ten grains of each were measured for each sample, as well as a few fusion crust measurements for the samples where it was present. Using the reference standards, the data were corrected using a single reference standard, as well as linearly, using three reference standards bracketing the data. There was found to be almost no discernable difference between the two methods.

Further analysis of the selected samples allowed them to be grouped into three textural groups, each with a different presumed history based on petrographical evidence. ALHA 81001 and NWA 1000 were described as impact melts. While they had very different grain sizes, they both had elongate, overlapping grains with no organized structure or orientation, consistent with a quenched texture. BTN 00300, EET 920020, LEW 85305, GRA 98098, and NWA 1923 were grouped based on their granular or granoblastic texture. They had more equidimensional grains, fairly uniform grain size, and abundant triple-junctions, evidence that they experienced significant thermal metamorphism. Finally, CMS 04049, PCA 91245, and QUE 97053 were grouped for their subophitic textures. Consisting of elongate, touching plagioclase grains, with pyroxene in between, this classic basaltic texture means that this group of samples likely experienced the least alteration from its original crystallization.

Analysis of the major element abundances aligned well with previously published data for plagioclase and pyroxene in eucrites. Trace elements were analyzed using typical incompatible trace element diagrams, normalized to CI chondrite values. In general, the samples displayed very similar ITE patterns, varying by about an order of magnitude. For the plagioclase grains, this pattern was a slight negative slope, enriched in the more compatible elements, and depleted in the less incompatible elements. All plagioclase grains showed positive Eu and Sr anomalies, and were depleted in the moderately volatile elements Cs, Zn, Rb, and Pb. For pyroxene grains, the general pattern was a slight positive slope, depleted in the more incompatible elements, and enriched in the less incompatible elements. All pyroxene grains show negative Eu and Sr anomalies, and significant depletions in the moderately volatile elements Cs, Zn, K, Rb, and Pb. NWA 1923 had anomalously low abundances across the board.

Bulk rock concentrations were reconstructed, assuming that plagioclase and pyroxene comprised 100% of the sample, and compared to actual bulk rock data from Dhaliwal et al. (in review). While this method omitted many minor accessory phases, the reconstructions showed only minor differences to the bulk data. The reconstructions were slightly depleted in the most incompatible elements, but successfully recreated the bulk abundances in the less incompatible elements. The general pattern for the bulk data and these reconstructions is a very flat ITE pattern at about 10 times chondritic abundances, and depleted in the moderately volatile elements Cs, Zn, K, Rb, and Pb. This bulk rock data was also almost identical to the fusion crust measurements taken in this study, confirming its usefulness as a proxy for bulk rock data.

Finally, moderately volatile abundances were analyzed two ways. The first method looked at the ratio between a moderately volatile element and a refractory element that behave similarly. Albarède (2014) used lunar volcanic glass to do this analysis, but this study was interested in determining whether individual minerals could serve the same purpose. Rb/Ba and Rb/Sr were used to analyze the plagioclase data. Rb/Ba showed Rb depletion levels similar to the Moon, and Rb/Sr showed depletion compared to the Earth, but might be just showing the signal of Sr enrichment. Zn/Fe was used to analyze pyroxene data, which also showed depletion levels similar to the Moon, while bulk values showed it slightly less depleted than the Moon.

The second method of assessing moderately volatile abundances involves the volatility trend visible when plotting normalized elemental abundances versus a measure of the element's volatility. Both 50% condensation temperature and bond energy (from Albarède et al. (2014)) were used as a measure of element volatility. In both cases, the refractory elements have consistent normalized abundances of ~1 at high 50% T_C and bond energies, and the volatile elements fall along a downward trend, with the slope of this trend indicating the level of

volatiles present. From these graphs it is clear that the Moon is much more depleted than Earth, and that eucrites fall somewhere in between.

6. Future Work

In order to continue the research in this study, it would be useful to measure a greater number of eucrites, as well as diogenites, to get a more complete picture of Vesta's crust, and see whether volatile depletions exist in those samples. Howardites would not be as useful because they are very likely to be contaminated. Additionally, more sensitive methods such as secondary ionization mass spectrometry (SIMS) or electron probe microanalysis (EPMA), could be used to find and measure the volatile contents of apatite, mesostasis, and other accessory grains, which would be more likely to actually contain the volatile elements and compounds that were estimated using moderately volatile elements in this study. Further calculations and analysis could give a quantitative value for the total volatile abundances of Vesta.

While NWA 1000 was grouped with ALHA 81001 as an impact melt in this study, its texture is unique enough to warrant further study. Using radiometric dating to get an accurate age for NWA 1000 would help greatly. A young age would imply that it is an impact melt, and an age in line with the rest of the eucrites might suggest another method of formation.

As mentioned in the discussion of the T_{50} and bond energy volatility graphs, the dataset published by Albarède (2014) was incomplete, and although attempts were made in this study to overlap and provide as much correlation as possible between the eucrite and lunar glass data, a more complete dataset would provide more accurate results.

Finally, the methods used in this study of measuring individual mineral grains using LA-ICP-MS or a similar method, could be used on many other types of samples. Primarily, a similar analysis of pyroxene and plagioclase grains on lunar basalts would test the arguments made in this study that individual mineral measurements can successfully recreate the bulk rock abundances, and be used to estimate volatile abundances using the moderately volatile elements.

References

Albarède, F., Albalat, E., & Lee, C. (2014). An intrinsic volatility scale relevant to the Earth and Moon and the status of water in the Moon. *Meteoritics & Planetary Science*, *50*(4), 568-577. https://doi.org/10.1111/maps.12331

Barrat, J., Blichert-Toft, J., Gillet, P., & Keller, F. (2000). The differentiation of eucrites: The role of in situ crystallization. *Meteoritics & Planetary Science*, *35*(5), 1087-1100. https://doi.org/10.1111/j.1945-5100.2000.tb01495.x

Barrat, J., Yamaguchi, A., Greenwood, R., Bohn, M., Cotten, J., Benoit, M., & Franchi, I. (2007). The Stannern trend eucrites: Contamination of main group eucritic magmas by crustal partial melts. *Geochimica Et Cosmochimica Acta*, *71*(16), 4108-4124. https://doi.org/10.1016/j.gca.2007.06.001

Binzel, R., & Xu, S. (1993). Chips off of Asteroid 4 Vesta: Evidence for the Parent Body of Basaltic Achondrite Meteorites. *Science*, *260*(5105), 186-191. https://doi.org/10.1126/science.260.5105.186

Bogard, D., & Garrison, D. (2003). ^{39}Ar-^{40}Ar ages of eucrites and thermal history of asteroid 4 Vesta. *Meteoritics & Planetary Science*, *38*(5), 669-710. https://doi.org/10.1111/j.1945-5100.2003.tb00035.x

Crozaz, G., & Wadhwa, M. (2001). The terrestrial alteration of saharan shergottites Dar al Gani 476 and 489: a case study of weathering in a hot desert environment. *Geochimica Et Cosmochimica Acta*, *65*(6), 971-977. https://doi.org/10.1016/s0016-7037(00)00586-x

Crozaz, G., Floss, C., & Wadhwa, M. (2003). Chemical alteration and REE mobilization in meteorites from hot and cold deserts. *Geochimica Et Cosmochimica Acta*, *67*(24), 4727-4741. https://doi.org/10.1016/j.gca.2003.08.008

Day, J.M.D. (2015). Planet formation processes revealed by meteorites. *Geology Today*, *31*(1), 12-20. https://doi.org/10.1111/gto.12082

Day, J.M.D., Brandon, A., & Walker, R. (2016). Highly Siderophile Elements in Earth, Mars, the Moon, and Asteroids. *Reviews In Mineralogy And Geochemistry*, *81*(1), 161-238. https://doi.org/10.2138/rmg.2016.81.04

Day, J., Taylor, L., Floss, C., Patchen, A., Schnare, D., & Pearson, D. (2006). Comparative petrology, geochemistry, and petrogenesis of evolved, low-Ti lunar mare basalt meteorites from the LaPaz Icefield, Antarctica. *Geochimica Et Cosmochimica Acta*, 70(6), 1581-1600. https://doi.org/10.1016/j.gca.2005.11.015

De Sanctis, M., Ammannito, E., Capria, M., Tosi, F., Capaccioni, F., & Zambon, F., F. Carraro, S. Fonte, A. Frigeri, R. Jaumann, G. Magni, S. Marchi, T. B. McCord, L. A. McFadden, H. Y. McSween, D. W. Mittlefehldt, A. Nathues, E. Palomba1, C. M. Pieters, C. A. Raymond, C. T. Russell, M. J. Toplis, D. Turrini (2012). Spectroscopic Characterization of Mineralogy and Its Diversity Across Vesta. *Science*, *336*(6082), 697-700. https://doi.org/10.1126/science.1219270

Dhaliwal, J., Day, J.M.D., & Tait, K. (in review). Petrogenesis of eucrites and diogenites without the requirement of a magma ocean. *Meteoritics And Planetary Science*.

Dhaliwal, J., Day, J.M.D., & Moynier, F. (2018). Volatile element loss during planetary magma ocean phases. *Icarus*, *300*, 249-260. https://doi.org/10.1016/j.icarus.2017.09.002

Elkins-Tanton, L. (2012). Magma Oceans in the Inner Solar System. *Annual Review Of Earth And Planetary Sciences*, *40*(1), 113-139. https://doi.org/10.1146/annurev-earth-042711-105503

Fu, R., Weiss, B., Shuster, D., Gattacceca, J., Grove, T., & Suavet, C. et al. (2012). An Ancient Core Dynamo in Asteroid Vesta. *Science*, *338*(6104), 238-241. https://doi.org/10.1126/science.1225648

Halliday, A., Lee, D., Porcelli, D., Wiechert, U., Schönbächler, M., & Rehkämper, M. (2001). The rates of accretion, core formation and volatile loss in the early Solar System. *Philosophical Transactions of The Royal Society of London. Series A: Mathematical, Physical and Engineering Sciences*, 359(1787), 2111-2135. https://doi.org/10.1098/rsta.2001.0901

Hans, U., Kleine, T., & Bourdon, B. (2013). Rb–Sr chronology of volatile depletion in differentiated protoplanets: BABI, ADOR and ALL revisited. *Earth and Planetary Science Letters*, 374, 204-214. https://doi.org/10.1016/j.epsl.2013.05.029

Hsu, W., & Crozaz, G. (1996). Mineral chemistry and the petrogenesis of eucrites: I. Noncumulate eucrites. *Geochimica Et Cosmochimica Acta*, 60(22), 4571-4591. https://doi.org/10.1016/s0016-7037(96)00277-3

Hublet, G., Debaille, V., Wimpenny, J., & Yin, Q. (2017). Differentiation and magmatic activity in Vesta evidenced by 26Al-26Mg dating in eucrites and diogenites. *Geochimica Et Cosmochimica Acta*, *218*, 73-97. https://doi.org/10.1016/j.gca.2017.09.005

Hyde B.C., Day J.M.D., Tait K.T., Ash R.D., Holdsworth D.W., Moser D.E. (2014) A study of weathering and heterogeneous mineral phase distribution in brachinite Northwest Africa 4872. *Meteoritics and Planetary Science*, 49, 1141-1156.

Lugmair, G., & Shukolyukov, A. (1998). Early solar system timescales according to 53Mn-53Cr systematics. *Geochimica Et Cosmochimica Acta*, 62(16), 2863-2886. https://doi.org/10.1016/s0016-7037(98)00189-6

Lodders, K. (2003). Solar System Abundances and Condensation Temperatures of the Elements. *The Astrophysical Journal*, *591*(2), 1220-1247. https://doi.org/10.1086/375492

Mandler, B., & Elkins-Tanton, L. (2013). The origin of eucrites, diogenites, and olivine diogenites: Magma ocean crystallization and shallow magma chamber processes on Vesta. *Meteoritics & Planetary Science*, 48(11), 2333-2349. https://doi.org/10.1111/maps.12135

Mayne, R., McSween, H., McCoy, T., & Gale, A. (2009). Petrology of the unbrecciated eucrites. *Geochimica Et Cosmochimica Acta*, *73*(3), 794-819. https://doi.org/10.1016/j.gca.2008.10.035

McCord, T., Adams, J., & Johnson, T. (1970). Asteroid Vesta: Spectral Reflectivity and Compositional Implications. *Science*, *168*(3938), 1445-1447. https://doi.org/10.1126/science.168.3938.1445

McDonough, W., & Sun, S. (1995). The composition of the Earth. *Chemical Geology*, *120*(3-4), 223-253. https://doi.org/10.1016/0009-2541(94)00140-4

McQuaig, D. R., Simon, J. I., Mittlefehldt, D. W., Armytage, R. M. G. (2019). Petrographical and Geochemical Investigations of Stannern Group Eucrites. *50th Lunar and Planetary Science Conference*. Abstract #3000. https://www.hou.usra.edu/meetings/lpsc2019/pdf/3000.pdf

McSween, H., Binzel, R., De Sanctis, M., Ammannito, E., Prettyman, T., Beck, A., Reddy, V., Le Corre, L., Gaffey, M.J., McCord, T., Raymond, C. A., Russell, C. T., & the Dawn Science Team. (2013). Dawn; the Vesta-HED connection; and the geologic context for eucrites, diogenites, and howardites. *Meteoritics & Planetary Science*, *48*(11), 2090-2104. https://doi.org/10.1111/maps.12108

McSween, H., Mittlefehldt, D., Beck, A., Mayne, R., & McCoy, T. (2010). HED Meteorites and Their Relationship to the Geology of Vesta and the Dawn Mission. *Space Science Reviews*, *163*(1-4), 141-174. https://doi.org/10.1007/s11214-010-9637-z

Mittlefehldt, D. (2015). Asteroid (4) Vesta: I. The howardite-eucrite-diogenite (HED) clan of meteorites. *Geochemistry*, *75*(2), 155-183. https://doi.org/10.1016/j.chemer.2014.08.002

Mittlefehldt, D., & Lindstrom, M. (1991). Generation of abnormal trace element abundances in Antarctic eucrites by weathering processes. *Geochimica Et Cosmochimica Acta*, *55*(1), 77-87. https://doi.org/10.1016/0016-7037(91)90401-p

Moynier, F., Day, J., Okui, W., Yokoyama, T., Bouvier, A., Walker, R., & Podosek, F. (2012). Planetary-scale strontium isotopic heterogeneity and the age of volatile depletion of early solar system materials. *The Astrophysical Journal*, 758(1), 45. https://doi.org/10.1088/0004-637x/758/1/45

Neumann, W., Breuer, D., & Spohn, T. (2014). Differentiation of Vesta: Implications for a shallow magma ocean. *Earth and Planetary Science Letters*, 395, 267-280. https://doi.org/10.1016/j.epsl.2014.03.033

Paniello, R., Moynier, F., Beck, P., Barrat, J., Podosek, F., & Pichat, S. (2012). Zinc isotopes in HEDs: Clues to the formation of 4-Vesta, and the unique composition of Pecora Escarpment 82502. Geochimica Et Cosmochimica Acta, 86, 76-87. https://doi.org/10.1016/j.gca.2012.01.045

Pringle, E., & Moynier, F. (2017). Rubidium isotopic composition of the Earth, meteorites, and the Moon: Evidence for the origin of volatile loss during planetary accretion. *Earth and Planetary Science Letters*, 473, 62-70. https://doi.org/10.1016/j.epsl.2017.05.033

Righter, K., & Drake, M. (1997). A magma ocean on Vesta: Core formation and petrogenesis of eucrites and diogenites. *Meteoritics & Planetary Science*, 32(6), 929-944. https://doi.org/10.1111/j.1945-5100.1997.tb01582.x

Sarafian, A.R., John, T., Roszjar, J. and Whitehouse, M.J., 2017. Chlorine and hydrogen degassing in Vesta's magma ocean. *Earth and Planetary Science Letters*, 459, pp.311-319.

Sarafian, A., Nielsen, S., Marschall, H., Gaetani, G., Righter, K., & Berger, E. (2019). The water and fluorine content of 4 Vesta. *Geochimica Et Cosmochimica Acta*, 266, 568-581. https://doi.org/10.1016/j.gca.2019.08.023

Sarafian, A., Nielsen, S., Marschall, H., McCubbin, F., & Monteleone, B. (2014). Early accretion of water in the inner solar system from a carbonaceous chondrite-like source. *Science*, *346*(6209), 623-626. https://doi.org/10.1126/science.1256717

Sarafian, A., Roden, M., & Patiño-Douce, A. (2013). The volatile content of Vesta: Clues from apatite in eucrites. *Meteoritics & Planetary Science*, *48*(11), 2135-2154. https://doi.org/10.1111/maps.12124

Stolper, E. (1977). Experimental petrology of eucritic meteorites. *Geochimica Et Cosmochimica Acta*, 41(5), 587-611. https://doi.org/10.1016/0016-7037(77)90300-3

Thaisen, K., & Taylor, L. (2009). Meteorite fusion crust variability. *Meteoritics & Planetary Science*, 44(6), 871-878. https://doi.org/10.1111/j.1945-5100.2009.tb00774.x

Trinquier, A., Birck, J., Allègre, C., Göpel, C., & Ulfbeck, D. (2008). 53Mn–53Cr systematics of the early Solar System revisited. *Geochimica Et Cosmochimica Acta*, 72(20), 5146-5163. https://doi.org/10.1016/j.gca.2008.03.023